POLITECNICO DI TORINO

Collegio di Ingegneria Chimica e dei Materiali

Master of Science
in Materials Engineering for Industry 4.0

Master's Degree Thesis

Surface structure of TiO_2-anatase (001) films

Tutors

Dr. Maurizio De Santis
Prof. Mauro Tortello
Dr. Xavier Torrelles

Candidate

Tchouta Duvier Dzeubou

Session July 2025

Abstract

The main objective of this six months internship was to grow TiO_2-anatase (001) layers on top of substrates such as strontium titanate, $SrTiO_3$, and study and optimize their structure. Films were grown by Molecular Beam Epitaxy (MBE) deposition technique. This was achieved by optimizing the deposition parameters and conditions.

Once the deposition is done, the surface structure is analyzed using the Low Energy Electron Diffraction (LEED), while chemical composition and the presence of contaminants was investigated by Auger Electron Spectroscopy (AES).

The experimental set-up allowing to record and analyze quantitative LEED has been implemented only at the end of the internship and it was not possible to record the intensity of LEED diffraction spots versus electron energy. On the other hand, a film was studied by surface x-ray diffraction, recording a full data set for determining the structure. This data analysis is beyond the objective of this internship. The earlier mentioned experimental methods were employed to examine films grown on various substrates under diverse physical conditions.

The research seeks to achieve an in-depth understanding of how atoms are organized on the surface of these specifically oriented TiO_2-anatase films grown on particular substrates.

This understanding is important for optimizing the potential applications of these films, particularly in photocatalysis, where the TiO_2-anatase (001) is newsworthy due to its photocatalytic behavior.

The results obtained during this internship demonstrate the effectiveness of using MBE to deposit TiO_2-anatase (001) thin films with well-aligned crystalline structures on various substrates under controlled conditions. LEED analysis allowed to examine the surface structure and atomic arrangement, demonstrating the influence of the substrate on the orientation and quality of the film. Auger Spectroscopy identified the chemical composition, revealing the presence of titanium, oxygen and traces of iridium, providing essential information on any defects and contaminants. Different deposition parameters, such as substrate temperature and oxygen pressure, showed a significant impact on the film quality, with oxygen crackers improving oxidation and reducing defects. Finally, the observed surface reconstructions were consistent with theoretical models [1] [2] and confirmed the epitaxial orientation of the films, in agreement with previous studies on thin film growth.

Acknowledgment

First and foremost, I am very grateful to my supervisor, Dr. Maurizio De Santis, for providing me with the priceless opportunity to work on this project. Your continuous availability and patience in reiterating concepts that I struggled to assimilate have not only enriched my knowledge but also stimulated my curiosity to learn more about the topic that was previously unknown to me. Thanks to Dr. Xavier Torrelles for his suggestions throughout this work.

I am grateful to Prof. Mauro Tortello for having accepted to follow my work from the very beginning, even before we meet in person. I truly appreciated his engagement and clarity in explaining what needed improvement, qualities that made our collaboration pleasant.

Thank you to all my friends at Politecnico for these unforgettable years, especially Jospin and Franklin. Appreciation to my non-PoliTo friends, Leo, Edo, and Lore for their friendship.

A thank you goes to the Cho-Beni family, who have truly been my family here in Turin over these years, offering support and a sense of belonging. Heartfelt gratitude to Maman Minette.

I want to thank my brother Gabriel Kamdem Youbissi for his dynamism, always-positive attitude and good advice.

Many thanks to my sister Drousile Boufang Dzeubou, who, despite being in the USA, has always been there to support and encourage me, thank you from the bottom of my heart.

I am deeply thankful to my mother, Gisele Leopold Sayou, my number one fan and the first person to lift my spirits whenever things are tough, thank you for your endless love and encouragement.

My deepest thanks to my father and example, Francois Dzeubou, the architect of the man I am today, the one who showed me the right path and continues to give me the best advice in all aspects of life, helping me grow and improve every day. I owe you everything.

Finally, I give gratitude to the God of Bandenkop and to my ancestors, especially: Benoit Mangwa, Ma'a Ngouotou and Ta'a Nzeubou for accompanying me through this long, challenging and beautiful path. I always count on you! Guè pin.

Contents

List of Figures

List of Tables

1 Introduction

Institut Néel is named after Louis Néel, the institute pays tribute to the French physicist, winner of the Nobel Prize in physics in 1970 for his discoveries on antiferromagnetism and ferrimagnetism.

The institute was established in Grenoble in 2007 as a reorganization of several pre-existing CNRS laboratories (Centre de Recherches sur les très basses températures, Laboratoire d'étude des propriétés électroniques des solides, Laboratoire Louis Néel and Laboratoire de cristallographie).

The Néel Institute participates in the management of the French F-CRG (Collaborating Research Group) beamlines at the ESRF (European Synchrotron Radiation Facility) which are exploited by researchers from all over the world. [3]

This internship was conducted within the SIN (Surfaces, Interfaces and Nanostructures) team belonging to the QUEST department.

The experimental set-up installed in the F102c room, consisting of two interconnected ultra-high-vacuum chambers equipped with MBE sources and LEED and Auger techniques was used.

The preliminary substrate annealing was carried out in an oven in an underground floor of the F building.

Complementary structural measurements were performed on the F-CRG on interfaces beamline (IF, also called BM32) at the European Synchrotron Radiation Facility (ESRF).

BM32 is a specialized beamline which utilizes X-rays (generated by the synchrotron) diffraction to conduct a wide range of investigations into the properties of materials.

It is equipped with a two-crystal monochromator which allows the production of monochromatic X-ray beams of a certain energy.

2 Material system

2.1 TiO_2

Known for its diverse applications, titanium dioxide or titania, with the chemical formula TiO_2, is an inorganic compound derived from titanium.

Titanium dioxide is a nontoxic, biocompatible, and inexpensive material with very high dielectric constant and chemical stability. It is a semiconductor with a wide bandgap ranging from 3.0 to 3.4 eV.

Depending on its chemical composition, this oxide could present various values of electrical conductivity mainly due to the presence of oxygen defects, while the contribution of intrinsic free carriers is negligible even at high temperatures.

Moreover, the high stability to corrosion, the low-cost production, and the nontoxicity makes it a good candidate as food additive.

Due to its electronic properties, TiO_2 has been largely studied and employed as photocatalyst (e.g., water splitting, self-cleaning surfaces, antimicrobial coatings, etc.). [4]

Titanium oxide can form under specific conditions of high pressure and high temperature but most of the time it is found naturally in mineral form.

In this last circumstance are found the main and best-known polymorphs of TiO_2 which are: rutile, anatase and brookite; anatase and rutile are the most commonly used polymorphs of titanium dioxide in industrial applications due to their unique properties that make them highly recommendable for a variety of uses.

Under ambient conditions, rutile is the most common and stable naturally occurring physical form of titanium dioxide; it possesses a clear, well-defined color that can be pale grey, reddish-brown, or even deep black in presence of impurities.

The discovery of natural rutile crystals was initially met with disappointment due to their impurities. However, the development of the Boule technique (crystal growth process) later yielded a single, large, colorless synthetic rutile crystal. [5]

The rutile crystal structure consists of Ti atoms that reside at the center of octahedral arrangements formed by oxygen, and each oxygen has three Ti atoms as neighbors.

Rutile crystallizes in a tetragonal unit cell, defined by lattice parameters of a=b=4.584 Å and c=2.953 Å, where a and b represent equal side lengths and c represents the height of the unit cell.

The way rutile TiO_2 interacts with its surroundings depends a lot on how its crystals are oriented. The flat surfaces of a crystal, called facets, each have their own unique set of

surface properties. The (110) facet is the most common and studied one, but there are even other facets like (100), (001), (101), and (011). [6]

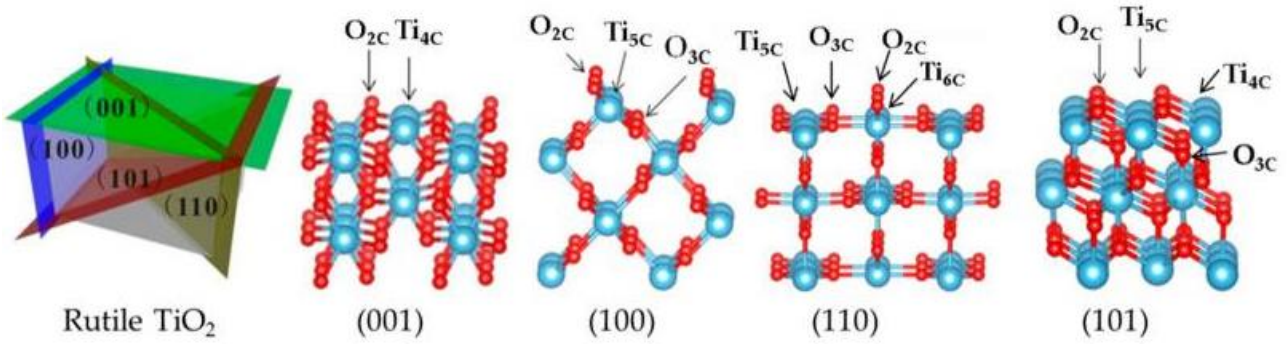

Figure 1: Side views of rutile TiO_2 (001), (100), (110), and (101) surfaces. Note: Ti, blue; O, red. [6]

Since at high temperatures rutile has the lowest Gibbs free energy of all the polymorphs of TiO_2 then it is all the most thermodynamically stable form at high temperatures; it is easily produced at these temperatures.

During the synthesis of TiO_2 at lower temperatures, the nucleation rate of anatase surpasses that of rutile. As a result, anatase crystals form more easily and appear in traces within igneous and metamorphic rocks; the reduced energy barriers for nucleation and growth contribute to anatase being the kinetically dominant phase.

Similar to rutile, anatase crystallizes within the tetragonal system where each titanium atom is coordinated by six oxygen atoms forming a slightly distorted octahedron; its lattice parameters are a=b=3.784 Å and c=9.513 Å.

Anatase displays a less rigid structure compared to rutile due to the variation of Ti-O bond lengths and because the O-Ti-O bond angles exhibit a small degree of distortion compared to the theoretical angles of a regular octahedron.

The difference in how atoms are arranged within the crystal structure leads to a clear distinction in density. Anatase is less dense, with a value of about 3.9 g/cm³, while rutile packs its atoms more tightly, resulting in a higher density of approximately 4.2 g/cm.

The anatase polymorph of titanium dioxide is widely recognized for its superior photocatalytic activity when compared to other polymorphs such as rutile and brookite. This enhanced performance is largely due to its slightly wider band gap, which allows for more efficient generation of electron-hole pairs under UV light. These electron-hole pairs are essential, as they drive the photocatalytic reactions by enabling oxidation and reduction

processes at the surface of the material. The larger band gap grants anatase a greater capacity to accept electrons from other molecules. This translates to a stronger oxidizing power, crucial for driving photocatalytic reactions.

Furthermore, when comparing materials for photocatalysis, a key factor is their specific surface area. A larger surface area provides more active sites where light-induced chemical reactions can take place, ultimately improving the material's overall efficiency. In this respect, anatase outperforms rutile, as it generally exhibits a significantly greater specific surface area, allowing for a higher density of reactive sites. [7]

Despite its advantages, however, anatase is less thermodynamically stable than rutile, making it more challenging to synthesize in a pure, single-phase form. Special techniques are needed to create pure anatase. [8]

The performance of anatase TiO_2 is facet-dependent, similar to rutile. Its exposed crystal planes, like (101), (001), (100), and (200), have distinct surface chemistry that influence how they interact with molecules. The (101) facet stands out for its exceptional photocatalytic activity, attracting significant research interest; this facet is the thermodynamically most stable surface and has a relatively low surface energy compared to other facets, making it the dominant exposed facet in most anatase crystals. It maintains a balanced relationship between reactivity and structural robustness during photocatalytic activities.

Based on theoretical calculations, the stability of anatase surfaces when exposed to gas or vacuum follows this order (most stable to least stable): (101) > (100) > (103)-faceted >= (001) > (103)-smooth > (110). [9]

The (001) facet has a higher surface energy (so more unstable) compared to the (101) facet, making it less stable but more reactive, as a matter of fact, the (001) facet of anatase TiO_2 stands out for its high reactivity which stems from a higher concentration of titanium and oxygen atoms that lack full atomic bonds. This reactivity is beneficial for photocatalytic reactions as it enhances the adsorption of reactants and the separation of photogenerated electron-hole pairs.

Investigating the (001) facet of anatase is a challenge due to its rarity in natural crystals, in fact, natural anatase crystals favor other facets, leaving the (001) facet with a measly 20% or less of the surface area. This low surface coverage makes it difficult to study and utilize the (001) facet in practical applications, as obtaining a sufficient quantity of these facets for detailed analysis and experimentation is somewhat complicated.

To overcome this hurdle, are employed synthesis techniques like fluorine treatment or hydrothermal methods which promote the formation and stability of the high-energy (001) facet, allowing for its closer examination. [10]

Hence, the anatase TiO_2 (001) facet is theoretically more efficient in photocatalysis, owing to its increased surface reactivity linked to a higher concentration of undercoordinated titanium and oxygen surface atoms. This configuration facilitates greater adsorption capacity and improved charge carrier dynamics. However, the high surface energy renders this facet thermodynamically unstable, thus requiring controlled synthetic techniques for stabilization. In contrast, the (101) facet emerges as the predominant surface in natural crystal growth due to its lower surface energy. It is widely adopted in photocatalytic applications as it provides a stable and cost-effective platform with sufficiently high activity, enabled by its balanced structural and chemical attributes.

Early research using Scanning Tunneling Microscopy (STM) to study the surface chemistry of a mineral containing anatase TiO_2 revealed fascinating differences in how various surfaces behave. The (101) surface seems to be the most stable, meaning its atoms stay put and don't rearrange themselves. In contrast, other surfaces, like the (100) surface, undergo reconstruction, changing their atomic arrangement.

Anatase (001) often displays a (4x1) reconstruction, a specific rearrangement of surface atoms. This altered surface structure significantly impacts the material's properties. In photocatalysis, the atomic arrangement on the surface is crucial because it affects how light interacts with the material and how efficiently photogenerated electron-hole pairs can be separated and utilized for chemical reactions. The (4×1) surface reconstruction, characterized by a repeating pattern every four units along one axis and one unit along the perpendicular direction, contributes significantly to enhancing the surface reactivity of anatase. This periodic arrangement increases the density of active sites available for photocatalytic processes, thereby improving the material’s overall performance. As a result, the precise atomic structure of the surface, including reconstructions like the (4×1), plays a fundamental role in influencing the photocatalytic efficiency of anatase. A deeper understanding and careful control of these surface configurations are essential for optimizing anatase in key applications, such as hydrogen generation and solar energy conversion. [11]

2.2 $SrTiO_3$

Formulated as $SrTiO_3$, strontium titanate is a basic inorganic material with excellent dielectric properties. The material's high dielectric constant enables it to hold a significant amount of electrical charge, which is particularly useful for applications like capacitors and devices that need high energy storage density.

Strontium titanate also known as STO at room pressure and temperature has a cube-shaped crystal structure (perovskite ABO_3) of Pm3m space group with a lattice parameter of 0.3905 nm and a density of ρ=5,12 g/cm^3, where titanium cations Ti^{4+} are located in the center of the unit cell, the oxygen anions O^{2-} are located in the center of each face and the strontium cations Sr^{2+} are situated at the corners of the cubes. This structure changes to a slightly distorted cube (tetragonal) of I4/ mcm space group at very low temperatures, around below -168.15 °C. [12]. The crystal is typically transparent but can be colored by doping specific rare earth or transition metal elements.

During the internship some Nb doped substrates were also employed. They are metallic, which is an advantage in experiments using electrons as probes.

Property	Value
Lattice parameter at RT (nm)	0.3905
Atomic density (g/cm^3)	5.12
Melting point (°C)	2080
Mohs hardness	6
Dielectric constant (ε_0)	300
Thermal conductivity (W/m.K)	12
Coefficient of thermal expansion (Å/°C)	9.4×10^{-6}
Refractive index	2.31-2.38

Table 1: Summary of the physical properties of $SrTiO_3$. [13]

Due to its high refractive index, strontium titanate is commonly employed in the fabrication of optical components and is particularly effective as a window material in the infrared spectral range. When these films are initially deposited, they tend to be in an amorphous, disordered state. However, subjecting them to high-temperature annealing, typically around 900 °C, induces a phase transformation into a polycrystalline structure, characterized by numerous small crystals that are often aligned along a preferred orientation. This thermal treatment also tends to produce a rough surface with clearly defined grain boundaries. Among the various surface terminations observed in $SrTiO_3$, the TiO_2-terminated surface is particularly well-studied, especially in the case of the (100) crystallographic orientation. This

specific termination significantly influences the surface's reactivity and is important in epitaxy, which is the way a film relates its structure with the substrate one. High-temperature treatments can induce reconstructions on the surface, which are crucial for applications in catalysis and electronics. Studying the surface of $SrTiO_3$ involves techniques like LEED, X-ray diffraction and scanning electron microscopy. [14]

Thanks to the lattice parameter compatibility, $SrTiO_3$ was used as substrate in the research for the growth of (001) oriented TiO_2-anatase films (misfit $\frac{a_{STO}-a_{TiO_2}}{a_{STO}}$ = 3% where a_{STO} is the lattice parameter of the substrate, i.e. the length of the side of the unit cell of $SrTiO_3$ and a_{TiO2} is the lattice parameter of the film that we want to grow on, in this case TiO_2 in anatase phase). [15]

2.3 ***LaAlO$_3$***

Another material used as a substrate for TiO_2-anatase films is lanthanum aluminate, $LaAlO_3$. Lanthanum aluminate stands out as the most important single crystal substrate for the growth of high-temperature superconducting thin films.

The band gap of $LaAlO_3$ is broad, typically falling between 4.6 to 5.6 electron volts. This significant gap between its valence band and conduction band designates it as a proficient insulator. Electrons must overcome a substantial energy barrier to transition across the band gap and enable electrical conductivity. [16] [17]

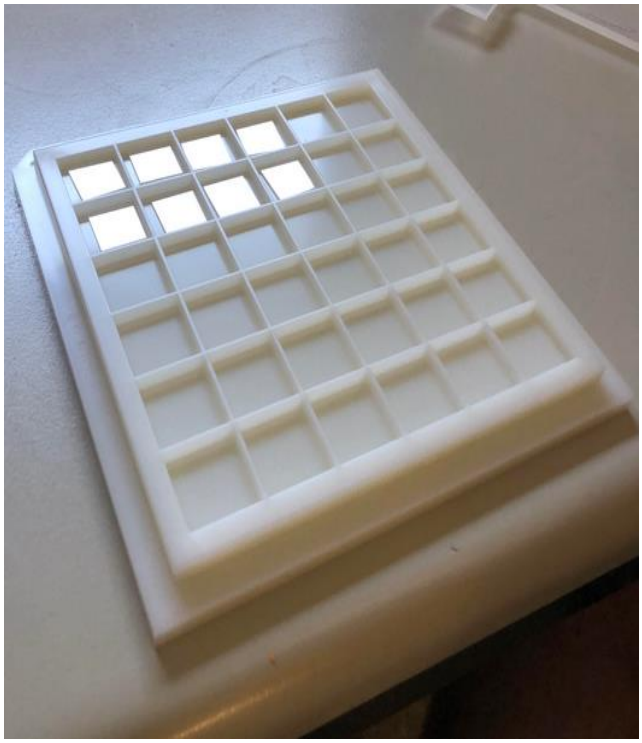

Figure 2 & 3: respectively The lid of the $LaAlO_3$ substrates container and the LaAlO3 samples themselves. [18]

The crystal structure of $LaAlO_3$ shows a subtle deviation from the ideal perovskite structure, which is typically characterized by a highly symmetrical cubic arrangement of atoms. While perovskites are often considered model systems due to their simple and regular geometry, $LaAlO_3$ exhibits a slight rhombohedral distortion. This distortion results in a minor elongation along one axis of the unit cell, leading to a structure that remains close to cubic in appearance but with a lower symmetry. At room temperature, the lattice parameter is approximately 3.787 Å, reflecting the near-cubic nature of the unit cell despite the small structural deviation. [19]

This leads to an excellent match with the in-plane lattice constant of anatase (001), with a lattice mismatch as low as 0.1%. Such a close match significantly reduces the formation of structural defects at the interface and promotes high-quality epitaxial growth of the overlayer. Surface oxygen vacancies are prevalent in $LaAlO_3$, significantly influencing its surface and interface properties. These vacancies play a key role in the observed insulator-to-metal transition within $LaAlO_3$ / $SrTiO_3$ heterostructures. Studies utilizing techniques like low-angle resonant soft X-ray scattering have revealed the coexistence of these vacancies with interface conducting states, critical for understanding the electronic behavior of the material. [20]

3 Experimental methods

3.1 Auger Electron Spectroscopy (AES)

Auger Electron Spectroscopy (AES) proves to be the most important non-destructive and semi-quantitative tool for analyzing the chemistry of surfaces. This technique relies on a phenomenon called the Auger effect.

The Auger effect showcases an interesting way atoms lose energy; when a core electron is missing, an electron from a higher shell fills the hole. But instead of radiating a photon, the excess energy can be transferred to another nearby electron of the same atom called bystander electron, causing its ejection because the energy released by the electronic transition (from the upper to the inner shell) exceeds the binding energy of the spectator electron. This ejected electron is the Auger electron. Its kinetic energy is characteristic of the element it comes from. [21]

For accurate analysis, AES operates in a high vacuum (less than 10^3 Pa) to eliminate interference from gas molecules. It then employs an electron beam to excite the sample and a detector to capture the resulting Auger electrons, providing valuable information about the surface composition.

AES excels at analyzing the very topmost layer of a material. This makes it ideal for studying issues like surface contamination, identifying unwanted elements clinging to the surface. Additionally, it can reveal segregation, where certain elements prefer to reside near the surface, and study the composition of thin films, ultra-thin layers deposited on a material's surface. AES is a highly surface-sensitive technique with detection limits around 0.1 atomic percent, making it effective for analyzing the top few atomic layers (0.4 -10 nm) of a material. [22]

The energy of an Auger electron, ejected during an “ABC” transition, can be estimated using a formula that involves the binding energies E of the electrons in the three levels (A, B, and C) involved. However, binding energies can change slightly depending on the presence of other vacancies in the atom. The basic formula is $E_{ABC} = E_A - E_{\mathrm{B}} - E_{\mathrm{C}}$ but for approximation, the following equation is used to calculate the kinetic energy of Auger electrons: $\mathrm{E_{ABC}} = \mathrm{E_A(z)} - \frac{1}{2}[\mathrm{E_B(z)} + E_B(\mathrm{z+1})] - \frac{1}{2}[E_{\mathrm{C}}(\mathrm{z}) + E_{\mathrm{C}}(\mathrm{z+1})]$ that uses an average of binding energies for levels B and C (adjusted slightly for neighboring elements, z+1). The z is the atomic number of the atom.

For exact calculation, other effects should be taken into account, such as the Coulombic

repulsion energy between two holes as well as the intra-atom and extra atom relaxation energies. Hence, $E_{ABC} = E_{final} - E_{initial}$, is the ultimate formula where E_{final} and $E_{initial}$ represent the total energy of the atom before and after the Auger emission. [23]

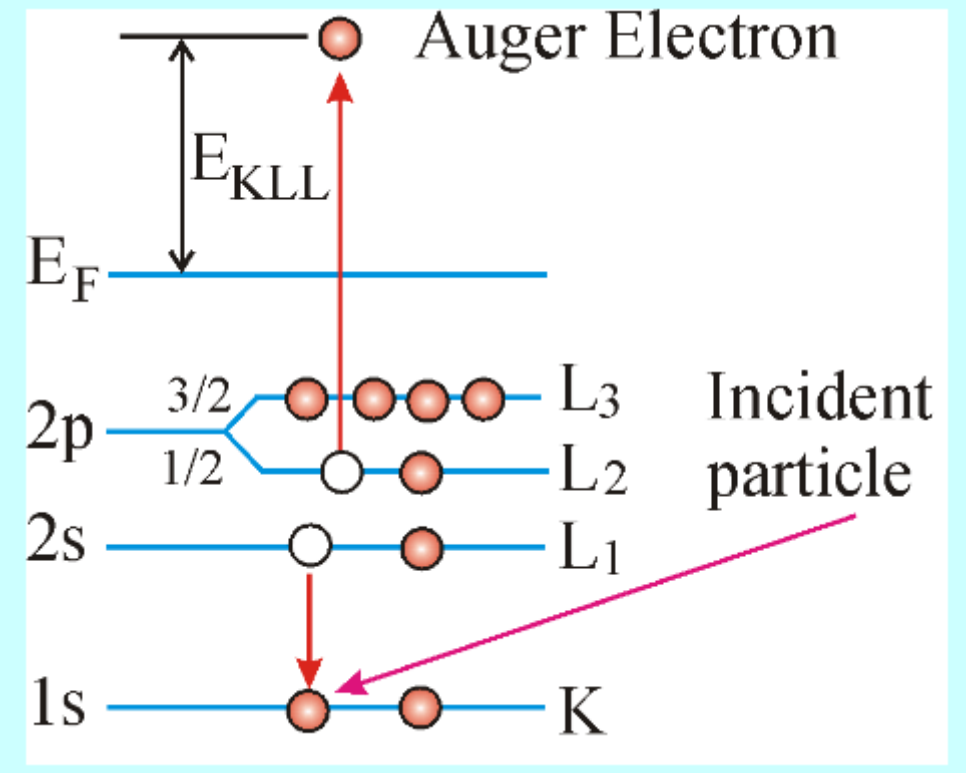

Figure 4: Estimation of Kinetic Energy. [23]

In Auger spectroscopy, electron shells are conventionally labelled K, L, M, and N to reflect increasing principal quantum numbers (n=1, 2, 3, 4). The principal quantum number n specifies the electron's main energy level, its typical distance from the nucleus (higher n values correspond to orbits farther out), and its overall energy state, notably in hydrogen-like atoms.

The K-shell (n=1), being the innermost electronic level, consists solely of the 1s subshell and exhibits the greatest electron binding energy as a consequence of direct nuclear proximity. Subsequent shells demonstrate increasing complexity: the L-shell (n=2) contains the 2s orbital along with spin-orbit split 2p orbitals ($2p_{1/2}$ and $2p_{3/2}$), while the M-shell (n=3) incorporates 3s, 3p, and 3d orbitals. This systematic organization of electronic states, extending to higher principal quantum numbers (N, O shells) in heavy elements, forms the

basis for understanding core-level excitations and decay processes in X-ray spectroscopy and electron emission phenomena.

Transitions involved in the Auger effect are identified by letter combinations such as KLL or MNN, which specify the origin and destination of electrons during the transition sequence. For instance, in a KLL transition, the initial vacancy is created in the K shell (n=1), an electron from the L shell (n=2) fills this vacancy, and another electron, also from the L shell, is emitted as the Auger electron. This notation reflects a three-step mechanism: initial core-level ionization, electronic relaxation, and electron emission. Each transition is element-specific and provides crucial information about the atomic structure and chemical state of the material's surface.

Hence, Auger transition labels not only describe the sequence of shell interactions but also provide insights into the energetics and elemental identity of the emitting atom. The characteristic kinetic energy of the emitted Auger electron serves as a fingerprint, allowing for qualitative and quantitative surface analysis.

3.2 Low Energy Electron Diffraction (LEED)

During the internship the low energy electron diffraction (LEED) technique was one of the main techniques used to determine the surface structure of the various samples tested.

LEED is frequently utilized to verify the cleanliness and organization of surfaces being set up for additional experiments. LEED experiments are conducted in conditions well-known where there is the absence of gasses and where we minimize electron interactions. The ultra-high vacuum (UHV) chamber maintains an extremely low pressure (typically below 10^{-12} Pa) environment to prevent contamination.

The technique of LEED uses electrons with low energy, typically between the values of 20 eV and 400 eV, and the wavelength of the electron beam is around 1 Å. The low energy is a very important detail because it increases the sensitivity of the method to the surface atoms, rather than the bulk material. [24] The low-energy electrons strike a crystalline surface scatter in specific directions defined by the periodic arrangement of surface atoms, resulting in a characteristic diffraction pattern. The LEED technique allows the determination of surface atomic arrangement through analysis of the generated diffraction patterns.

By examining these patterns, it is possible to obtain fundamental information regarding: the surface structure and atomic positions, the symmetry of the surface lattice (e.g., square, hexagonal), the degree of surface order, and any surface reconstructions induced by energy

minimization or external influences [25] [26].

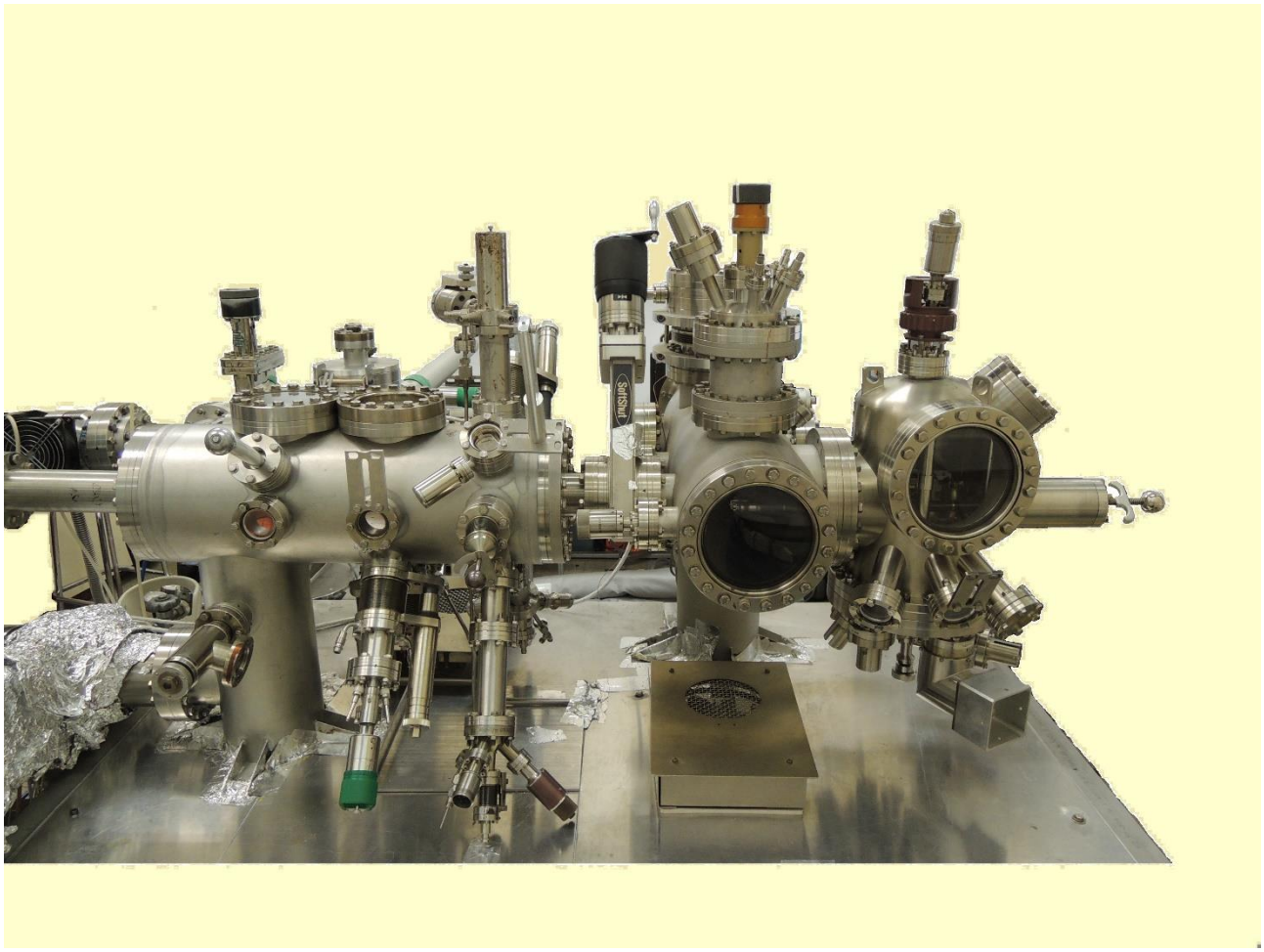

Figure 5: LEED machine in F102b room. [27]

In a LEED experiment, various components are required to ensure proper operation and accurate interpretation of the resulting diffraction patterns.

An electron gun produces a beam of low kinetic energy that is directed at the surface of the sample that we want to analyze. This electron gun is made by: a cathode, which is heated at high temperatures (1000°C - 2500°C) to create a stream of electrons, an anode that has the function of accelerate and further focus the beam and a set of focusing lenses which are electromagnetic lenses: components designed to manipulate the trajectory of the electron beam emitted from the cathode. Their primary function is to converge or diverge the beam to control its focus and enhance resolution.

The sample holder securely holds the sample in the desired position and allows accurate positioning and alignment within the experimental setup thanks to the rotation, tilt and

translation mechanisms that ensure that the electron beam can be directed towards a specific part of the sample. [24]

Without precise temperature control (allowed by heating/cooling systems), LEED experiments suffer from unreliable data due to variations in sample temperature.

Heating the sample can help remove contaminants such as adsorbed gasses or surface oxides by desorbing them from the surface. This is essential for obtaining a clean and well-ordered surface necessary for accurate LEED measurements. Cooling the sample may also help stabilize certain surface structures or phases that are only present at low temperatures.

Based on these considerations, it is essential to utilize a sample holder capable of withstanding ultra-high vacuum (UHV) conditions and accommodating potential heating or cooling scenarios to ensure the experiment remains unaffected by external factors.

As the electrons collide with the surface of the sample, they diffract in many directions depending on the surface crystallography. Once the electrons diffract, they head back towards three grids followed by a phosphor covered screen. The first grid is grounded and basically serves as a shield which protects the second grid as a result of its negative potential. The second grid acts as a filter by allowing only the electrons with higher energies to pass through. The lower energy electrons are blocked out, they result from inelastic scattering processes and give only a background signal. The third grid accelerate the elastic electrons on the screen (at high voltage, in the 4-7 keV range) [24]. The screen is typically coated with a phosphorescent material because converts incident electron impacts into visible light. When electrons strike the phosphor-coated surface, they induce luminescence, the intensity of which is directly proportional to the electron beam intensity. The resulting interference pattern formed by the luminescent spots corresponds to the crystal surface structure. These patterns constitute the images obtained through LEED analysis. [28]

Modern advancements in LEED instrumentation often incorporate Charge-Coupled Device (CCD) cameras alongside or as a substitute for the classic phosphor screens to record electron diffraction images. Therefore, CCD acts as a highly sensitive detector that converts the incoming electron-induced light signals into digital images with high resolution and low noise. Thanks to the slow scan CCD camera, the short period needed for data acquisition can be separated from the longer phases of digitization, storage, and analysis. The acquisition of a complete LEED dataset typically requires 30-40 minutes, with effective exposure times of 200-300 seconds (approximately 1 second per energy point) at a primary beam current of 100 nA [29]. This corresponds to a total dose of roughly 12 electrons per adsorbate particle, a value that can be further reduced if required, while maintaining sufficiently short durations to minimize contamination risks, even for highly sensitive surface

layers.

CCD-based detection is particularly useful for experiments that monitor structural changes over time, especially when surfaces are subjected to variations in temperature, gas atmospheres, or external electric and magnetic fields. [30]

Finally, to conclude everything we need a data acquisition and analysis software which collects, processes, and interprets diffraction pattern data and facilitates a detailed analysis. In our case we installed a set-up thanks to the collaboration with the team from TU-Wien, which develops the viperLEED code which is a comprehensive package aimed at making quantitative low energy electron diffraction easily accessible to the scientific community [31]. It comprises four main parts (conceptually independent from one another): measurement of LEED-I(V) “movies”, extraction of I(V) curves from LEED movies, calculations of theoretical I(V) curves based on a structural guess and optimization of the structure to best fit the experimental data. In this context, the term “movies” refers to a series of frames captured over a range of incident electron energies, emphasizing the dynamic aspect of data acquisition. This approach involves monitoring continuous or discrete variations in electron energy, resulting in a sequence of diffraction images that illustrate the evolution of the pattern as a function of energy. [32]

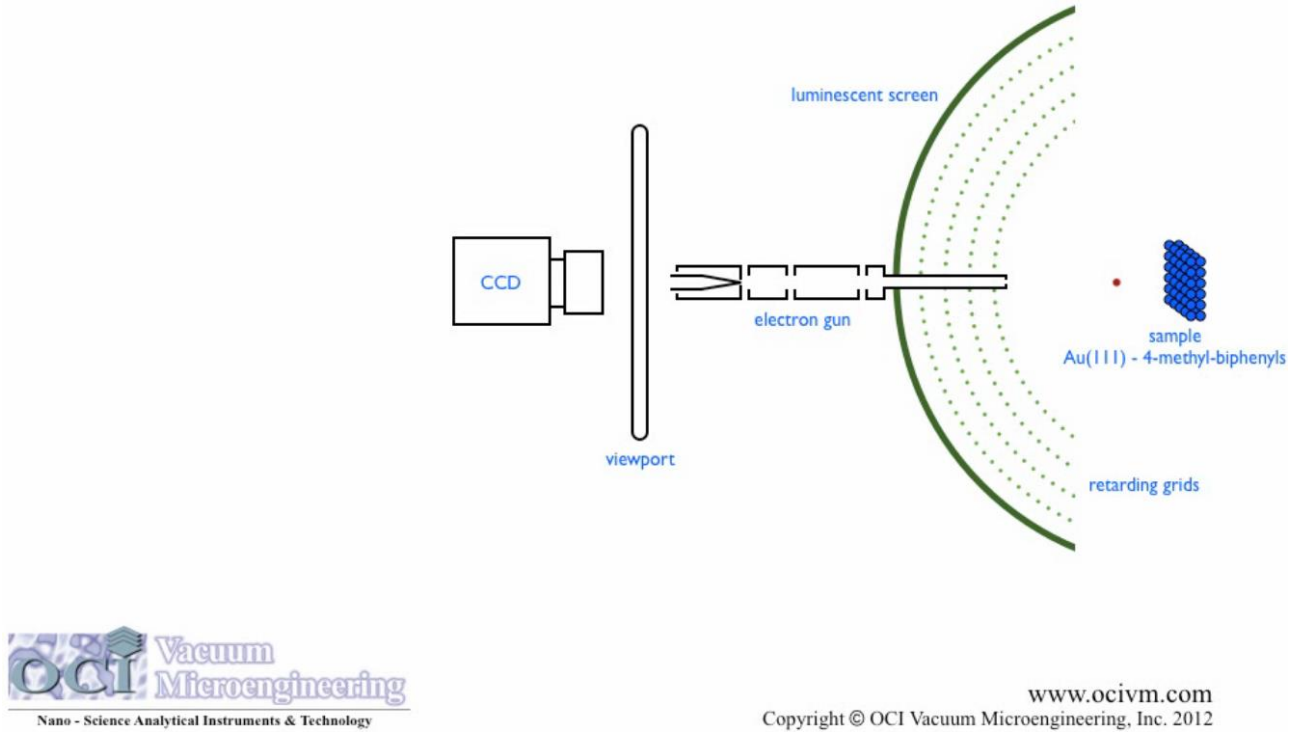

Figure 6: Low Energy Electron Diffraction Animation. [28]

During the internship we could not go through the full process of collecting images and extract the I(V) curves for data analysis. This step will be performed by the SIN team in the next few months. However, the data acquisition chain is now operational.

Nevertheless, LEED spot patterns can be analyzed to reveal details about surface symmetry, surface reconstruction, or surface defects such as steps and islands. They can also indicate whether surface molecules are adsorbed in an ordered or random fashion.

The LEED pattern is characterized by an array of spots (or beams) generated by the interference of electrons diffracted by the surface atoms of a crystalline material. These spots form a two-dimensional diffraction pattern, where their spatial arrangement, intensity distribution, and morphology provide critical insights into the surface structure of the sample under investigation. The distance between spots in a LEED diffraction pattern corresponds to the reciprocal lattice vectors of the crystal's surface, with the spacing determined by the lattice parameters of the crystal and the angle of incidence of the electron beam. A larger spacing between spots indicates a larger surface unit cell, whereas a smaller spacing reflects a smaller unit cell. The intensity of the spots provides insights into the symmetry and atomic arrangement of the surface layer. Higher-intensity spots signify stronger reflections from specific crystallographic directions, while variations in intensity may suggest surface reconstructions or the presence of defects.

Additionally, the shape of the spots reveals information about the quality and order of the crystal surface. Sharp, well-defined spots are characteristic of a highly ordered surface, whereas broader or diffuse spots may indicate disorder, surface roughness, or the presence of adsorbates.

The initial step in LEED analysis involves indexing the diffraction spots assigning them to specific crystallographic planes within the surface structure. This is achieved by comparing the experimental pattern with theoretical models or structural databases to identify the correct surface configuration. To understand how well the theoretical model describes the real data, an indicator called "reliability factor" or "R-factor" is used, which measures how close the calculation results are to those of the experiment. A lower R-factor reflects a higher degree of agreement, and thus, greater confidence in the accuracy of the determined crystal structure.

LEED has made important contributions, but it still shows regular differences between experimental and theoretical results, even with simple surfaces. The theory shouldn't be expected to fit every detail perfectly. In fact, forcing a perfect fit could lead to misleading interpretations, since you're likely adjusting the model to match noise rather than meaningful data. [24]

Systematic variation of the electron beam's incident angle enables determination of surface orientation, since angular changes induce corresponding modifications in the diffraction pattern. More precise atomic structural information is achieved through LEED I-V curves, where diffracted spot intensities are measured versus electron energy. The behavior of these I-V curves offers deeper insights into the atomic-scale surface structure, aiding in the optimization of theoretical surface models.

Moreover, the method can identify various surface imperfections like missing atoms or adsorbed molecules. These defects reveal themselves through distinct signatures in the diffraction pattern, including intensity variations, new spot formation, or changes in spot profile, all of which provide diagnostic information about surface quality.

A concrete and illustrative example of how a LEED pattern (the array of spots observed on the LEED screen) corresponds to the surface crystal structure is provided by considering a simple surface such as the (100) face of a cubic crystal (e.g., Cu). In this case, the surface of the crystal is assumed to be cut parallel to the (100) plane, resulting in a regular, periodic arrangement of atoms on the surface. The LEED pattern produced by such a surface will display a systematic grid of diffraction spots, reflecting the symmetry of the atomic arrangement underneath. The spacing between the spots corresponds to the inverse of the atomic spacing in the surface layer, and the pattern will exhibit fourfold symmetry, as the atoms are arranged in a square pattern.

If the surface remains pristine and unaffected by reconstruction, meaning it was cleaned carefully by various cycles of sputtering with ions of argon followed by annealing, the pattern will be clear and symmetric. Any discrepancies from this idealized pattern, such as additional or shifted spots, may indicate surface reconstruction or imperfections in the atomic configuration. By analyzing the LEED pattern, it becomes possible to extract detailed information about the surface structure, including atomic spacing, layer positioning, and potential surface relaxations.

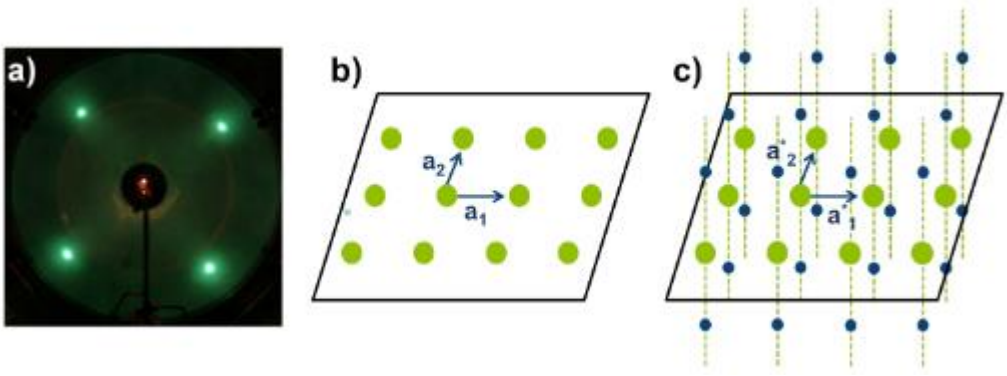

Figure 7: (a) LEED pattern of Cu (100) surface, (b) 2D atomic layer (real space), and its (c) reciprocal lattice. [33]

Due to the hemispherical shape of the LEED fluorescent screen, the reciprocal lattice can be observed without distortion. It is crucial to note that the distance between points in the reciprocal lattice is inversely related to the actual interplanar spacing; in other words, when atoms are farther apart, the spots in the diffraction pattern move closer together, and vice versa. For the superlattices, which consist of alternating layers of two different materials, new diffraction points emerge in addition to the original pattern.

Hence, the diffracted beams of electrons hit a fluorescent screen, forming a pattern of light spots that directly corresponds to a scaled version of the reciprocal lattice of the crystal's unit cell which is a collection of theoretical points, with vectors between them aligning with the normal to atomic planes in real space. For example, as the electron beam penetrates several atomic layers, the reciprocal lattice observed in LEED manifests as continuous rods and discrete points corresponding to each atomic layer. While LEED patterns provide information about the size and geometry of the real space unit cell, they do not indicate the atomic positions. To determine these positions, an analysis of the diffraction spot intensities is necessary.

LEED reveals surface reconstructions, which are the reconfigurations of atoms occurring in the topmost layers of a crystal. These surface-specific structures emerge because the chemical and physical surroundings at the surface differ significantly from those experienced by atoms within the bulk. Within the bulk of a material, atoms are generally enclosed by a complete set of neighboring atoms, creating stable and energetically optimal arrangements. In contrast, surface atoms, missing neighbors on one side, experience an imbalance in bonding forces. This imbalance often causes the surface atoms to reorganize themselves to lower the system’s total free energy. [34]

When a surface undergoes reconstruction, it frequently forms a periodic arrangement distinct from the structure of the bulk material beneath it. The resulting surface unit cell may be enlarged, reduced, rotated, or otherwise altered compared to the original bulk cell. These transformations are not arbitrary but are driven by the material’s need to optimize atomic bonding, relieve surface stress, adapt to adsorbed molecules, or react to external influences like changes in temperature or pressure. Surface reconstructions can range from minor atomic displacements to more complex phenomena, such as the creation of vacancies, the appearance of adatom arrays, or the development of entirely new two-dimensional structures.

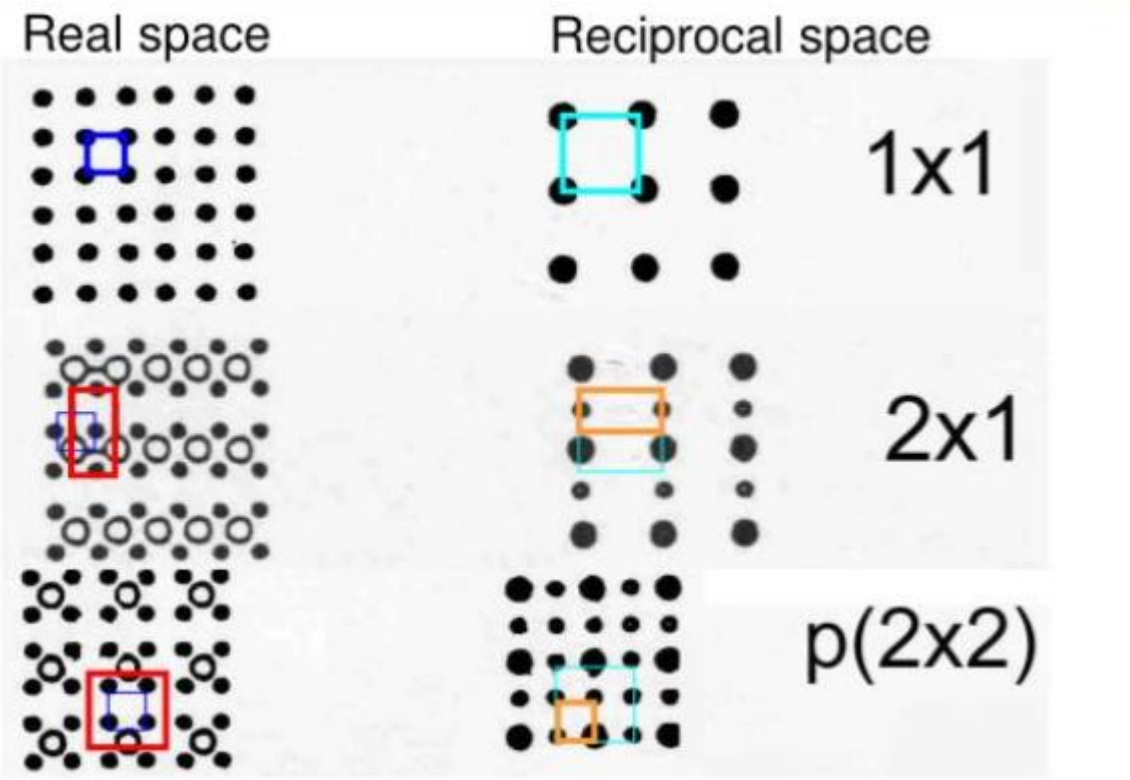

Figure 8: Real space and reciprocal space. [35]

The Figure 8 presents a comparison between two different ways of representing surface structures: real space and reciprocal space. On the left side of the figure, we see the arrangement of atoms in real space, which is simply how the atoms are positioned in the material. This shows us the actual layout of the surface atoms and how they are spaced relative to each other. On the right side, the same surface structures are shown in reciprocal space, which is a mathematical representation used in diffraction studies. Reciprocal space helps us understand how the surface atoms interact with an electron beam in techniques like LEED (Low-Energy Electron Diffraction). It provides insight into the periodicity and symmetry of the surface by showing diffraction spots, which are the result of electron scattering.

In Figure 8 are displayed three surface configurations: a) 1x1 structure represents a basic, simple surface where the atoms are arranged in a regular, repeating pattern with a straightforward periodicity. It's an example of an "unreconstructed" surface, meaning there hasn't been any significant change to the atom arrangement at the surface compared to the bulk material beneath it; b) 2x1 reconstruction: In this case, the atomic arrangement is more complex. The pattern shows a doubling of the periodicity in one direction, meaning that the surface atoms have reorganized themselves. This is often due to surface reconstructions, where atoms move to a more stable configuration to lower the surface energy; c) p(2x2)

reconstruction is another example of a reconstructed surface, but here the atoms are arranged in a slightly different pattern. The p(2x2) notation indicates that the surface atoms form a periodic structure that is also doubled in one direction, but with a different arrangement than the 2x1 pattern. This could be caused by surface relaxation or the presence of adsorbed molecules that influence the atomic arrangement.

Several physical and chemical processes can drive surface reconstruction, depending on the surrounding environment of the material.

One common pathway is thermal activation, where high temperatures, particularly in a gaseous atmosphere, supply enough energy for surface atoms to migrate and reorganize into lower-energy configurations, differentiating the surface structure from that of the bulk.

Electrochemical stimulation represents another mechanism, wherein applying a specific electric potential to the solid can modify atomic bonding forces at the surface, prompting structural reorganization.

Lastly, chemical interactions occurring at relatively low temperatures can induce surface reconstruction. Here, reactions between the material and reactive species can destabilize the original surface arrangement, leading atoms to adopt a more stable structural order.

Surface relaxation, in other hand, involves relatively slight changes in the locations of atoms near a surface, compared to their perfect bulk lattice positions. These displacements are typically along the axis normal to the surface. Often, this results in minor contractions or expansions of the first few interlayer distances, aiming to minimize the surface energy generated by unsatisfied bonds. Crucially, the surface maintains the same in-plane symmetry as the bulk material.

In an experiment conducted on a thin film of $SrTiO_3$, a surface reconstruction called ($\sqrt{13} \times \sqrt{13}$)-R33.7° was observed, in addition to the basic (1×1) structure. This atomic rearrangement is often induced by thermal treatments or particular growth conditions during thin film deposition. [36]

3.3 Molecular Beam Epitaxy (MBE)

Molecular Beam Epitaxy (MBE) is a method used to create extremely thin crystal layers, depositing them one atomic layer at a time onto a base surface known as a substrate.

This process takes place in an ultra-high vacuum environment to ensure the materials remain uncontaminated. In MBE, atoms or molecules are heated until they evaporate into a beam and move toward the substrate. Once there, the atoms gently settle and attach, forming a crystal layer that is both highly pure and precisely controlled. Because the atoms arrive at the surface very slowly, researchers can finely tune the layer-by-layer growth, achieving structures that are only a few atoms thick. MBE enables the production of exceptionally pure, high-performance materials, essential for technologies such as fast microchips, lasers, quantum computing components, and advanced sensors.

A defining advantage of Molecular Beam Epitaxy is its capability to create single-crystal layers with atomic-level precision. In MBE, films are built up one atomic layer at a time, typically progressing at a slow, controlled rate of one to three microns per hour. These ultra-thin structures serve as the foundation for many advanced semiconductor technologies, including high-speed integrated circuits, lasers, and lightwave system detectors.

Today, MBE is considered the top method for growing crystal films, allowing scientists to build semiconductor structures that aren't possible with natural materials or older techniques. Thanks to its unmatched precision and flexibility, it has expanded possibilities in materials and device engineering. [37]

For the stage experiments, MBE epitaxy was the chosen method for growing TiO_2 layers on the diverse substrates. This approach enables the creation of well-defined crystalline thin films.

MBE is conducted in an ultra-high vacuum setup, maintaining pressures below ~ 10^{-8} Pa, which is necessary to ensure that no extraneous molecules contaminate the developing thin film. To achieve a clean internal environment, the chamber is baked at high temperatures (140°C) to remove any adsorbed gas.

Prior to achieving a clean and well-ordered surface, the substrate undergoes thorough cleaning to eliminate contaminants, followed by high-temperature treatment for desorption of any residual contaminants.

In the Molecular Beam Epitaxy process, effusion cells play a crucial role, functioning similarly to guns that emit controlled beams of atoms or molecules toward a substrate. These cells are specially designed containers where high-purity materials are placed for deposition. When the effusion cells are carefully heated to the appropriate temperatures, the solid material inside gradually evaporates, releasing a beam of atoms or molecules into the ultra-

high vacuum environment of the MBE chamber. [38]

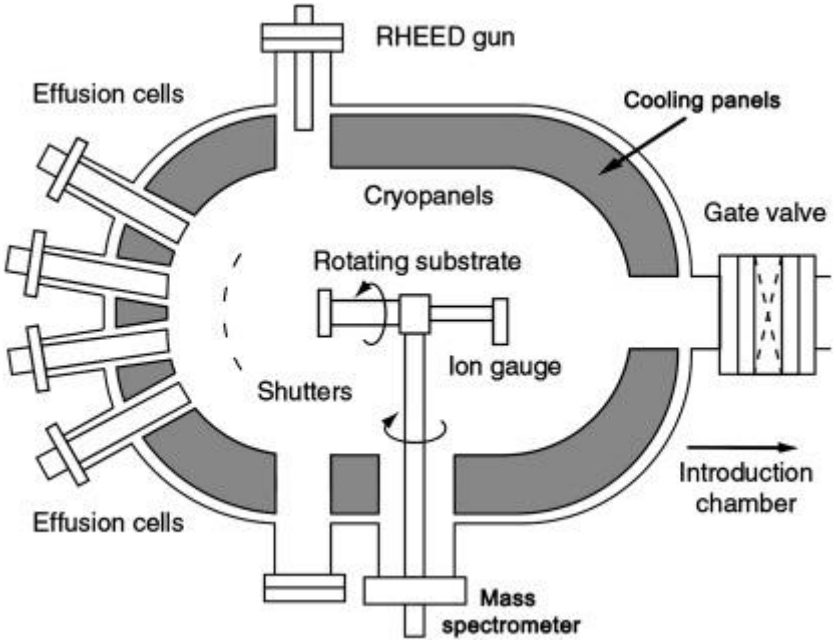

Figure 9: Scheme of MBE system. [39]

Residual gases in MBE chambers primarily originate from the chamber's inner walls, often due to insufficient baking prior to deposition. Additional gas molecules are released from heated components inside the chamber, including effusion cells, substrate holders, and shutter blades exposed to high temperatures. To minimize contamination, these parts must undergo thorough degassing before growth begins. The total pressure of residual gases is monitored using ionization gauges, while a mass spectrometer identifies specific gas species and their concentrations. [38]

The primary function of these effusion cells is to thermally evaporate the solid source material and deliver a steady and directed flux of atoms or molecules onto the surface of the substrate, enabling the growth of thin films with atomic-layer precision. The material flux needs to be precisely controlled to ensure uniform and high-quality crystal growth. Therefore, to accurately determine and monitor the deposition rate (flux) from each effusion cell, calibration tools such as a beam flux monitor or a quartz crystal microbalance are employed. These devices measure the number of atoms or molecules reaching the substrate per unit time, allowing fine-tuning of the growth conditions.

Maintaining precise control over the flux is essential because it directly influences the thickness, composition, and overall structural quality of the deposited layers. In summary, effusion cells are vital components in MBE, ensuring that the materials are delivered in a

highly controlled, stable, and reproducible manner to achieve the desired film properties. [40] The substrate receives beams of atoms or molecules released from heated effusion cells. These atoms move in straight trajectories and condense upon contact with the surface, gradually forming a thin film.

This process enables epitaxial growth, meaning that each deposited atomic layer is perfectly aligned with the crystal structure of the substrate beneath it, ensuring exceptional precision in building materials one monolayer at a time. During the growth, in-situ monitoring techniques such as Reflection High-Energy Electron Diffraction (RHEED) are employed to continuously observe the surface. RHEED works by directing a high-energy electron beam at a very shallow angle onto the surface, producing diffraction patterns that give detailed, real-time information about surface smoothness, crystallinity, and growth rate.

By closely monitoring and analyzing changes in the RHEED patterns in real time, researchers can make immediate adjustments to key growth parameters, such as temperature, deposition rate and flux ratios. Through continuous monitoring and instant corrections, this feedback system maintains strict control over epitaxial growth, resulting in superior film quality.

Once the deposition phase is complete, the system undergoes a carefully controlled cooling process under ultra-high vacuum (UHV) conditions. This slow, gradual cooling minimizes thermal stress and prevents contamination from residual gases, thereby preserving the structural and chemical integrity of the thin film. Maintaining UHV conditions throughout this phase is critical to avoid defects or unwanted reactions at the film's surface.

Finally, advanced surface analysis techniques are employed to confirm the film's structural and compositional properties. LEED provides information on surface crystallography and long-range order, while Auger Electron Spectroscopy (AES) offers detailed chemical composition analysis with high surface sensitivity. Additionally, Scanning Tunneling Microscopy (STM) can be used to examine atomic-scale surface morphology and electronic structure, ensuring that the grown film meets the desired specifications. [41]

3.4 Scanning Tunneling Microscopy (STM)

Scanning Tunneling Microscopy (STM) is a powerful high-resolution imaging technique classified under scanning probe microscopy (SPM). Unlike conventional optical microscopes, which are constrained by the diffraction limit of light, STM overcomes these limitations by exploiting quantum tunneling to achieve atomic resolution.

Tunneling is a quantum mechanical effect where electrons can pass through a potential barrier, even if they classically do not have enough energy to overcome it. In classical mechanics, an electron would be blocked by the barrier if it lacks the necessary energy to surpass it. However, quantum mechanics reveals that electrons exhibit wave-like properties. These waves extend beyond the barrier, and if the barrier is thin enough, there is a non-zero probability that an electron will tunnel through it. This phenomenon, where electrons move through the barrier and emerge on the other side, is referred to as quantum tunneling.

The STM capitalizes on this quantum behavior, where the tunneling current is directly related to the wavefunctions of the electron at the tip of the microscope and the sample surface. By applying a bias voltage between the sharp probe tip and the surface, electrons tunnel through the atomic barrier, and the resulting current is measured. This allows STM to visualize and manipulate individual atoms on conductive or semiconductive surfaces with unprecedented resolution.

For optimal performance, STM is typically operated in an ultra-high vacuum environment, which minimizes surface contamination and unwanted interference from gas molecules.

The instrument's exceptional sensitivity relies on detecting minute variations in tunneling current, which flows between the atomically sharp metallic tip and the sample surface when a bias voltage is applied. To maintain a stable tunneling gap (typically less than 1 nm), STM employs advanced feedback control systems that continuously adjust the tip's position with picometer precision. This level of control, combined with the ability to scan surfaces in constant current or constant height mode, makes STM an indispensable tool in nanotechnology, surface science, and materials research.

Scanning Tunneling Microscope (STM) is composed of several key components: a sharp probe tip, typically made of tungsten (W) or platinum-iridium (Pt–Ir) alloy, which is essential for achieving the extremely close proximity required for quantum tunneling to occur; a piezoelectric scanner that precisely moves either the sample or the tip to enable scanning of the surface; a tunneling current detection system that measures the tiny current flowing between the tip and the sample; and a feedback loop that constantly adjusts the tip-sample distance to maintain a stable tunneling current, ensuring accurate imaging at the atomic scale. The piezoelectric scanner itself is made up of three independent piezoelectric

transducers aligned along the x, y, and z axes. By applying a sawtooth voltage to the x-piezo and a ramp voltage to the y-piezo, the tip is able to systematically scan the surface in the xy-plane. Fine vertical adjustments are controlled through the z-piezo, which allows the system to position the tip and sample within a fraction of a nanometer from each other.

During operation, a bias voltage is applied between the tip and the sample. At such close distances, the electron wavefunctions of the tip and the sample begin to overlap, enabling electron tunneling and generating a measurable tunneling current. The feedback loop plays a crucial role by dynamically adjusting the tip's height to keep the tunneling current constant, thereby allowing the STM to construct a highly detailed image of the sample's surface. [42] This tunneling current, which depends on the tip-sample separation, is measured to create a detailed map of the surface. A feedback loop maintains a constant tunneling current by adjusting the tip height via a piezoelectric scanner. These height adjustments are recorded to generate a topographical map. Data collected on the tunneling current and tip height is processed by STM software to generate a high-resolution 3D surface image. The images are analyzed for properties like atomic arrangement and electronic states, and additional measurements like spectroscopy assess electronic properties such as density of states and work function. [43] During the internship only preliminary STM measurement were done, which are not reported in the following.

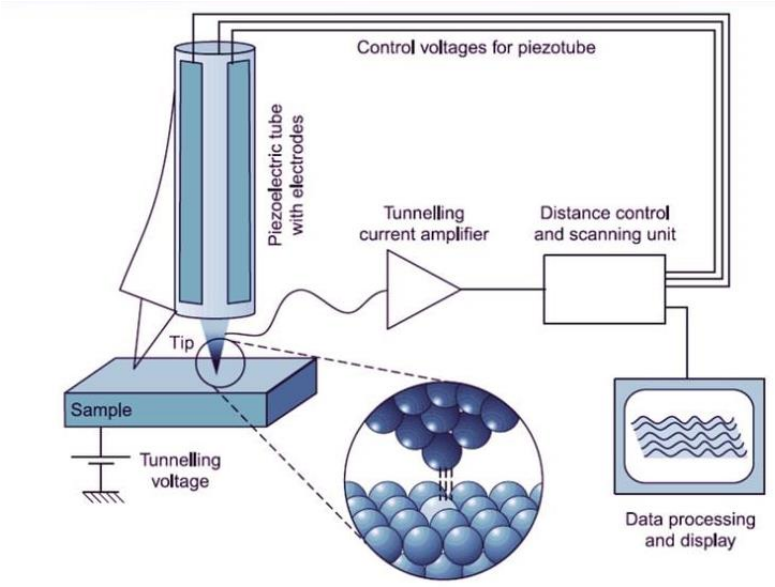

Figure 10: Scheme of STM system. [44]

3.5 X-Ray Diffraction (XRD)

X-ray diffraction (XRD) is a highly versatile, non-destructive analytical technique used to investigate the crystalline structure of materials. At its core, XRD relies on the principle of constructive interference of X-rays scattered by the periodic arrangement of atoms within a crystal lattice. When a beam of X-rays strikes a crystalline sample, the scattered waves produce distinct diffraction patterns only when they satisfy the Laue condition: $(k_l - k_0) * A_h = h$, where h is an integer related to the diffraction order, A_h corresponds to the orientation of atomic planes within the crystal, k_l and k_0 are the wave vectors of the scattered and incident X-rays, respectively. By analyzing the diffracted intensity as a function of all possible orientations relative to the incident beam, XRD can reveal information about the various orientations of atomic planes within the crystal. [45]

Typically, the X-ray diffraction (XRD) process involves several essential components working together to analyze the crystalline structure of a material. The system includes an X-ray source, which emits electromagnetic radiation with wavelengths on the order of angstroms, comparable to the typical spacing between atoms in crystalline solids. This specific wavelength range makes X-rays particularly effective for probing atomic arrangements and generating diffraction patterns.

The generation of X-rays is achieved through the rapid deceleration of highly accelerated electrons, a process typically facilitated by an X-ray tube comprising two electrodes: a negatively charged cathode (electron emitter) and a grounded anode (target). Within the cathode, a tungsten filament is resistively heated, thereby emitting electrons via thermionic emission. These electrons are then accelerated toward the anode by a high-voltage potential, usually in the range of 20-60 kV. Upon collision with the anode, the electrons' kinetic energy is partially converted into X-ray photons, primarily through bremsstrahlung radiation and characteristic radiation processes. The entire generation process is enclosed in a vacuum-sealed glass tube to minimize scattering and ensure efficient electron transport. Although X-rays are emitted isotropically from the anode, only a collimated beam, exiting at a shallow angle to the target surface, is utilized for diffraction experiments. A beryllium window, chosen for its minimal absorption of X-rays, allows the useful radiation to exit the tube while maintaining the internal vacuum. [46]

The material under investigation, usually prepared as a powder, thin film, or single crystal, is positioned so that its internal structure can interact with the incident X-ray beam. The detector is responsible for capturing the diffracted X-rays. By measuring the intensity and angular distribution of the diffracted beams, it provides critical data necessary for reconstructing the material’s crystallographic structure.

A key mechanical component of the setup is the goniometer, a precision rotational stage that allows the sample and detector to be moved relative to the incident beam. This controlled movement enables the collection of diffraction data over a range of angles, facilitating analysis of different lattice planes within the crystal. In more advanced laboratory configurations, not only the sample and detector but also the X-ray source itself can be rotated, providing access to specialized diffraction geometries such as grazing incidence, transmission, or reflection modes, depending on the experimental requirements and the type of structural information desired.

XRD offers numerous advantages compared to other analytical techniques. It can quickly, accurately, and non-destructively determine the mineralogical composition, phase identification, crystallinity, and even lattice strain in a sample. Another significant benefit is that sample preparation requirements are often minimal. In many cases, samples can be analyzed in their natural form or with only basic preparation, making the technique highly practical and efficient for both research and industrial applications. Furthermore, XRD is versatile enough to be applied to a wide range of materials, from metals and ceramics to polymers and biological specimens.

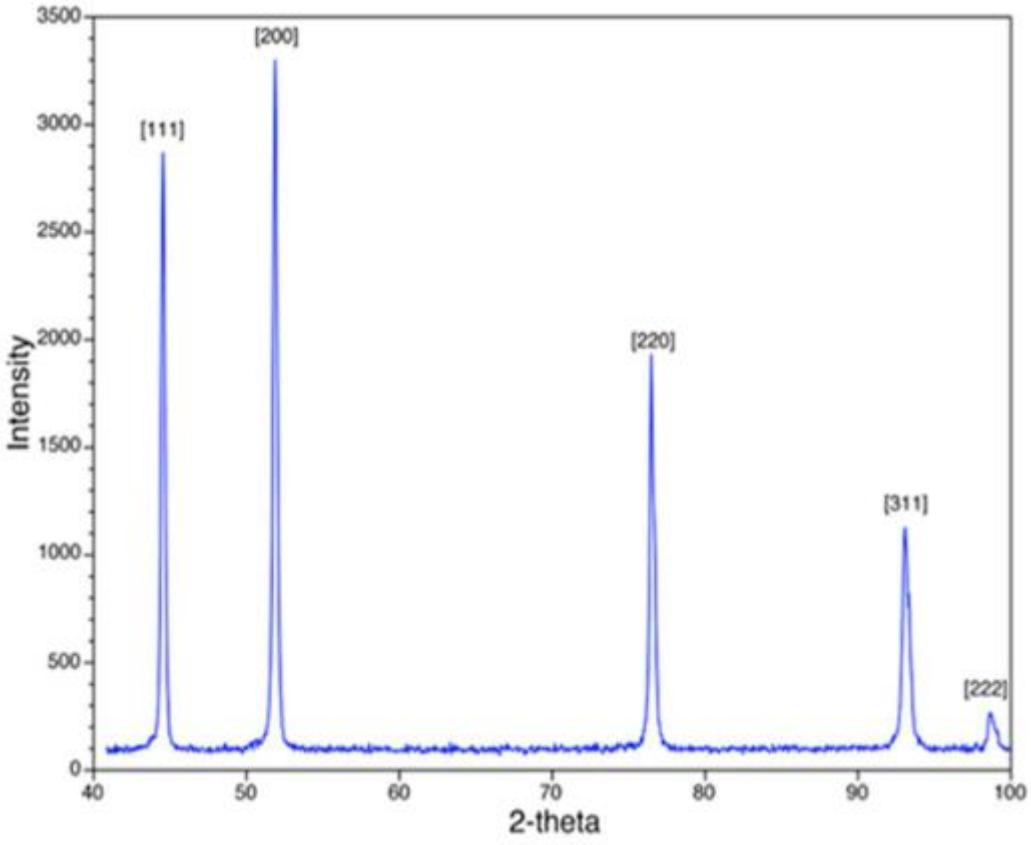

Figure 11: Example of the XRD pattern of Ni powder. [47]

X-ray diffraction (XRD) data interpretation is considered relatively straightforward compared to many other analytical techniques. XRD results are typically presented in the form of a diffraction pattern, consisting of a series of peaks plotted as intensity versus the diffraction angle (2θ). Each individual peak corresponds to a specific interplanar spacing within the crystal, as determined by Bragg's law. The position and intensity of these peaks are directly related to the crystallographic structure of the material.

Each crystalline phase present in a sample generates a unique diffraction pattern, determined by its specific chemical composition and atomic arrangement. When analyzing a mixture, the resulting XRD pattern is essentially the superposition of the individual patterns from each phase. Thus, a set of diffraction peaks forms an identifiable "fingerprint" for each phase, allowing for rapid and accurate identification of the crystalline substances present in a sample.

Through systematic comparison of the observed diffraction peak positions (2θ values) and their relative intensities with standardized reference patterns contained in crystallographic databases (e.g., the X-ray Powder Diffraction File, PDF, or the International Centre for Diffraction Data, ICDD [48]), the phase composition of the material can be determined efficiently. The reference patterns are often represented graphically by vertical sticks, indicating the expected peak positions and relative intensities for known phases. A good match is indicated when the experimental peak positions and intensities align closely with the reference sticks. Minor mismatches in peak position and intensity are typically acceptable as experimental error, but significant discrepancies, particularly the absence of major reference peaks, can indicate that the presumed phase is not actually present. It is important to note that peaks close together should shift in the same direction if affected by systematic experimental factors, following a cosθ dependence. Over a broad angular range, this shift behavior can vary. Most diffraction data show peak doublets rather than single peaks due to the presence of Kα1 and Kα2 components; the Kα1 peak is typically twice as intense as the Kα2. At lower 2θ angles, the doublet may not be clearly resolved.

Beyond simple phase identification, additional valuable information can be extracted from careful analysis of the diffraction data. For instance, diffraction peak positions can be used to calculate unit cell lattice parameters, offering insight into interatomic distances. Any factor altering these distances, such as temperature variation, substitutional doping, or mechanical stress, will cause measurable shifts in peak positions. Crystallite size and microstrain within the material can also be inferred: nanocrystalline materials or samples with significant lattice

defects often exhibit peak broadening. [49] However, peak broadening analysis has limitations; above a certain crystallite size threshold, which depends on the resolution of the diffractometer, broadening effects become indistinguishable.

While qualitative phase identification based on peak positions is relatively direct, quantitative or semi-quantitative phase analysis requires more careful treatment. The relative intensities of peaks must be interpreted cautiously, as absolute intensities can vary significantly due to instrumental and experimental parameters. Therefore, intensities are normalized relative to the most intense peak (designated the “100% peak”) to mitigate these variations. It is generally recommended to report diffraction data using the interplanar spacing (d_{hkl}) and relative intensities, rather than 2θ angles and absolute intensities, as d_{hkl} is an intrinsic, instrument-independent material property derived from Bragg’s law.

In addition to phase composition, the observed peak list can be used to extract a variety of crystallographic and materials properties, including unit cell dimensions, crystal system (by indexing peaks and identifying systematic absences), crystallite size, microstrain, and even several engineering parameters. Peak areas provide a more reliable measure of intensity compared to peak heights, particularly when quantifying crystallite size or degree of microstructural disorder. Accurate interpretation of peak broadening requires careful separation of the contributions from crystallite size, microstrain, and instrumental effects.

Unlike other techniques that may require complex mathematical modelling, extensive data processing, or highly specialized expertise for interpretation, basic XRD pattern analysis can often be carried out with a fundamental understanding of diffraction principles. Access to reliable reference patterns or databases significantly simplifies the process, enabling both qualitative phase identification and, in some cases, semi-quantitative analysis without the need for advanced computational methods. [47]

4 ESRF & Synchrotron

In standard XRD setups, X-rays are generated using a laboratory X-ray tube. This involves directing high-energy electrons towards a metal target, typically copper or molybdenum. This interaction produces characteristic X-ray radiation specific to the target material. Synchrotron facilities offer a powerful alternative X-ray source. Electrons are accelerated (200 million electron-volts) using electric fields until they are traveling very close to the speed of light. The electrons then enter the booster synchrotron, a ring with a circumference of 300 meters, travel round this ring several thousand times, gaining a little more energy with every lap. Once they reach their final energy of 6 billion electron-volts (6 GeV), they are sent into the storage ring. Every 50 ms, the booster can send a bunch of 6 GeV into the storage ring. This approach leads to the generation of highly intense and collimated X-ray beams with a broader range of energies compared to conventional X-ray tubes.

The ESRF, the European Synchrotron Radiation Facility, is the world's most intense X-ray source and a center of excellence for fundamental and innovation-driven research in condensed and living matter science.

The ESRF produces X-rays 100 billion times brighter than the X-rays used in hospitals. These X-rays, endowed with exceptional properties, are produced by the high energy electrons that race around the storage ring, a circular tunnel measuring 844 metres in circumference. The ESRF operates 46 beamlines, or laboratories, each equipped with state-of-the-art instrumentation, and managed by highly qualified scientific and technical experts. [50]

In this internship the XRD measurements were done at ESRF of Grenoble on the BM32 beamline.

Synchrotron radiation is produced in dedicated storage rings where electrons (or positrons) are kept circulating at constant energy. The radiation produced is emitted tangentially to the electron orbit confined to a narrow cone with an opening angle of $\frac{1}{\gamma}$ around the instantaneous velocity. The characteristic features of the radiation depend on two key parameters:

1) the cyclic frequency ω_0 of the orbiting electron.

2) γ, the electron energy in units of the rest mass energy, $\gamma = \frac{E_e}{mc^2}$.

Typically, this gives an emission fan of γ^{-1}~ 1 milliradian (mrad). In addition to the radiation obtained from the bending magnets that keep the electron beam traveling in the circular

orbit, radiation is also produced from insertion devices such as wigglers or undulators situated in the straight sections of the storage ring. These devices use alternating magnetic fields to force the electron beam to follow an oscillating path. In a wiggler the radiation from different wiggles adds incoherently whereas in an undulator the electron produces coherent addition of the radiation from each oscillation. The emitted spectrum is very broad, ranging from the far infrared to the hard X-ray region. [51] [52]

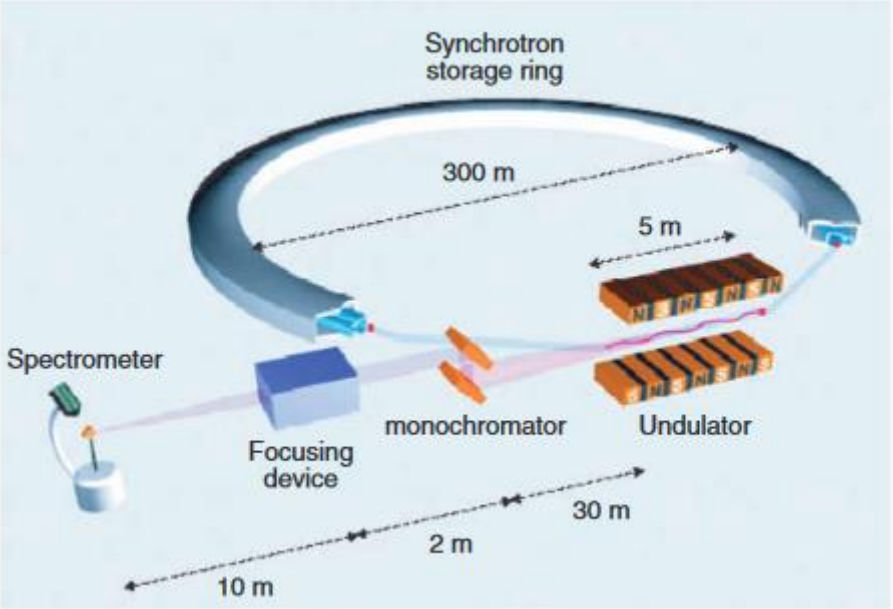

Figure 12: A schematic of a typical X-ray beamline at a synchrotron radiation source. [51]

Synchrotron radiation is inherently advantageous to laboratory sources for several reasons: due to their high intensity, synchrotron X-rays collect high-quality diffraction data in a shorter time frame compared to conventional sources. This allows for faster analysis and quicker scientific progress. The exceptional brightness and coherence of synchrotron X-rays contribute to superior resolution in diffraction experiments. This translates to more precise structural details being revealed compared to conventional X-ray sources. This enhanced precision is crucial for in-depth analysis of material structures. Unlike conventional sources with limited X-ray energies, synchrotron radiation offers a continuous spectrum. This tunability allows researchers to select specific X-ray wavelengths (energies) for their experiments. This optimization of X-ray energy based on the material of interest enhances both contrast (highlighting specific features) and resolution (detail level) in diffraction experiments.

The intense and focused beams of synchrotron X-rays make it possible to perform in-situ (real-time) studies of dynamic processes such as phase transitions, chemical reactions, and

mechanical deformation under various environmental conditions (temperature, pressure, atmosphere). [53]

Synchrotron facilities often offer complementary techniques such as X-ray absorption spectroscopy (XAS) and small-angle X-ray scattering (SAXS), which can provide additional information about the electronic structure and morphology of materials. The intense X-rays from synchrotrons facilitate micro- and nano-diffraction. This allows researchers to analyze the crystal structure of individual grains or phases within heterogeneous materials. This provides valuable information about the local variations in composition and arrangement within the material.

In the framework of this internship, synchrotron radiation was employed to investigate the surface structure of anatase. Standard X-ray diffraction is used to study the bulk structure of crystalline materials. This is because the X-ray interaction with the matter is weak compared to that of electrons, and x-ray penetrates for several micrometers in a solid. The intense X-ray beam generated at ESRF allows the study of the surface structure, whose diffraction peaks are one million of times weaker compared to a Bragg peak, allowing for example the study of surface reconstructions.

5 Experimental procedure

The following section describes the experimental procedure of elaboration of different samples, along with their characterization. Multiple specimens were synthesized under different growth conditions to investigate the influence of specific parameters on the resulting material properties. Among the prepared samples, three were deemed highly representative and are examined in detail: TiO_2 on $SrTiO_3$(100) doped Nb (Sample STO_C26; with cracker), TiO_2 on $SrTiO_3$(100) doped Nb (Sample STO_E1; without cracker) and TiO_2 on $LaAlO_3$(100) (Sample LAO1).

To represent the preparation of the substrate, was chosen as an example the preparation of the $SrTiO_3$ substrate: Nb 0.5 wt% (100) supplied by Crystec GmbH. The preparation protocol is designed to ensure a well-defined TiO_2-terminated surface, which is critical for the subsequent deposition process and for achieving high-quality epitaxial growth.

The preparation of the specimen starts with ultrasonic cleaning of the $SrTiO_3$ substrate.

The entire process requires meticulous attention to avoid damaging or contaminating the substrate; notably, the active surface must never come into contact with metal tweezers or other hard items. The substrate is carefully handled using precision tweezers, holding it from the sides, and then immersed in a beaker filled with high-purity isopropyl alcohol.

The beaker is subsequently placed in an ultrasonic water bath, where the substrate undergoes sonication for approximately 15 minutes. Following this initial cleaning step, the substrate is transferred to a second beaker containing deionized water to eliminate any residual alcohol. It is then subjected to a second round of ultrasonic treatment for an extended duration of 30 minutes, with the bath maintained at a temperature of approximately 60 °C to enhance the removal of organic and inorganic contaminants.

Once the sonication process is completed, the substrates are carefully extracted and positioned on an alumina ceramic tray, which had previously been cleaned and pre-heated to eliminate possible surface impurities. The tray, now containing the cleaned substrates, is enclosed and introduced into a high-temperature oven. The annealing step is carried out under ambient atmospheric conditions at a maximum temperature of 1000 °C. The temperature is ramped up at a controlled rate of 4 °C per minute and subsequently ramped down at a rate of 5 °C per minute. The total duration of this thermal treatment is approximately six hours.

This high-temperature annealing process is critical to achieve a TiO_2-terminated surface on the $SrTiO_3$ substrate, as it promotes the reorganization of surface atoms and the elimination

of surface defects, thereby facilitating the epitaxial growth of high-quality TiO_2 thin films in the subsequent deposition steps.

The following tables show the details of the preparation of the three substrates.

Sample STO_C26	Sample STO_E1	Sample LAO1
Sonicated 15' in ethanol (RT or at 40°C)	Sonicated 15' in ethanol (RT or at 40°C)	Sonicated 10' in ethanol
Sonicated in deionized water, 30' to 60°C - 70°C	Sonicated in deionized water, 30' to 60°C - 70°C	30' in deionized water at 60°C - 70°C
Annealed 6 hours at 1000°C in air	Annealed 6 hours at 1000°C in air	Annealed 6 hours at 1100°C in air
Sonicated in deionized water, 30' to 60°C - 70°C	Sonicated in deionized water, 30' to 60°C - 70°C	Sonicated 3' in deionized
Annealed 2 hours at 1000°C in air	Annealed 2 hours at 1000°C in air	
Sonicated in deionized water, 3'	Sonicated in deionized water, 3'	

Table 2: Experimental data. [54]

Once the substrate has been extracted from the oven, it is immediately prepared for subsequent processing via the Molecular Beam Epitaxy (MBE) technique under ultra-high vacuum (UHV) conditions. At this stage, the sample undergoes additional thermal treatment aimed at further degassing and structural rearrangement. This is achieved through radiative heating, employing a high-temperature filament strategically positioned behind the tantalum sample holder. The radiative source facilitates a controlled annealing process, essential for eliminating residual contaminants and ensuring optimal surface cleanliness and crystallographic order, prerequisites for high-quality epitaxial growth.

The deposition phase begins with the preparation of the metallic source material, in this case titanium, which is introduced into a crucible composed of pyrolytic boron nitride (PBN). This material is selected due to its excellent thermal stability, high thermal conductivity, and resistance to thermal shock, which make it particularly suitable for high-temperature applications under vacuum. The PBN crucible is housed within a molybdenum liner, which serves a dual purpose: it provides structural support and plays a crucial role in the electron bombardment heating mechanism by facilitating efficient electron evacuation.

The heating of the source material is realized through a process known as electron bombardment, wherein electrons are accelerated and directed onto the molybdenum liner. The interaction between the high-energy electrons and the liner results in the transfer of

kinetic energy, which is subsequently converted into thermal energy through inelastic collisions. This localized heating mechanism ensures precise thermal control over the crucible and its contents, thereby enabling stable and reproducible evaporation conditions.

The electron bombardment system operates under a high-voltage regime, with an applied potential difference of approximately 1000 volts across the filament. A filament current of about 1.93 amperes is maintained, and particular care is taken to increase this current gradually. This precautionary measure is critical to preserving vacuum stability, as abrupt changes in current may result in pressure spikes or damage to sensitive components within the evaporator assembly. Furthermore, the emission current, defined as the flow of electrons emitted from the thermionically heated filament, is carefully regulated to a value near 50 milliamperes. This parameter is pivotal in achieving and maintaining the desired deposition rate, ensuring uniform film growth across the substrate surface.

To ensure the accuracy and reproducibility of the deposition rates, the evaporation process was carefully calibrated by employing a quartz crystal microbalance (QCM). This technique enables real-time monitoring of the mass of the material being deposited by measuring the shift in the resonance frequency of a vibrating quartz crystal, which is directly correlated to the thickness of the deposited film, as described in reference [55].

Throughout all deposition processes, the growth rate of titanium (Ti) was maintained at approximately 4 nm per hour. This consistent rate was crucial for achieving precise control over the thickness of the resulting titanium dioxide (TiO_2) layers.

For all investigated samples, the formation of TiO_2 was achieved by first depositing a thin layer of metallic titanium, approximately 5 nm in thickness, under a controlled partial oxygen pressure environment. During this process, the substrates were maintained at elevated temperatures to facilitate the oxidation of the Ti layer. This thermal treatment promoted the in-situ formation of a uniform TiO_2 layer with an estimated final thickness of about 10 nm, resulting from the reaction between Ti and oxygen.

The STO_C26 and STO_E1 samples were subjected to nearly identical preparation procedures under ultra-high vacuum (UHV) conditions. Specifically, both underwent an initial degassing stage conducted over several hours at a temperature of 300°C, followed by an annealing process lasting 30 minutes at approximately 800°C, in an oxygen partial pressure of 1×10^{-6} mbar.

During the subsequent deposition phase, the environmental conditions were maintained constant for both samples, with an oxygen pressure of 1×10^{-6} mbar and the substrate temperature stabilized around 750°C. The primary distinction between the two samples lies in the growth configuration employed for STO_C26, which was positioned in front of an

oxygen cracker during deposition.

This cracker consists of an iridium capillary heated to elevated temperatures (>1500 °C), capable of thermally dissociating molecular oxygen (O_2) into its atomic form (O). Atomic oxygen exhibits a significantly higher chemical reactivity compared to its molecular counterpart, thereby enhancing the oxidation efficiency of titanium during film growth. The cracker filament operates under an applied voltage of approximately 1100 V, resulting in a current of about 14 mA, which in turn raises the capillary temperature above 1500°C, sufficient for effective O_2 dissociation.

In parallel, the LAO1 sample underwent a similar UHV treatment protocol. This included degassing for several hours at 300°C, followed by annealing for 30 minutes at a temperature of 850°C in an oxygen atmosphere of 1.1×10^{-6} mbar. During the titanium deposition phase for this sample, the substrate temperature was maintained at 850°C, with an oxygen partial pressure of 1.2×10^{-6} mbar.

6 Results & discussion

6.1 Analysis of LEED patterns

The evolution of the surface structure can be systematically monitored through the sequence of Low-Energy Electron Diffraction (LEED) patterns acquired at different stages of the experimental process. LEED is a powerful technique that enables detailed analysis of the crystallographic order and surface periodicity of materials by observing the diffraction of low-energy electrons upon interaction with the surface atoms.

A fundamental principle of LEED is that the variation of the incident electron beam energy directly influences the effective sampling depth and the spatial resolution of the technique. Specifically, the energy of the electron beam determines the radius of the Ewald sphere, a geometric construct employed to interpret diffraction phenomena in reciprocal space. As the electron energy increases, the radius of the Ewald sphere also increases, thereby altering the number and geometry of the reciprocal lattice points that satisfy the diffraction condition and intersect the sphere.

Consequently, higher electron energies result in a greater number of observable diffraction spots, enhancing the ability to resolve fine features in the surface structure. This characteristic makes LEED particularly valuable for studying changes in surface order, reconstruction, and film growth.

In this paragraph, the LEED patterns acquired for both the clean substrates and those coated with titanium thin films are presented and analyzed. For each sample, diffraction patterns were recorded at multiple primary electron energies, specifically at 60 eV, 100 eV, and 150 eV. This energy range was selected to ensure a comprehensive characterization of the surface periodicity and to allow comparison between the pristine and modified surface states. The resulting patterns provide insight into the degree of crystallinity, possible reconstructions, and the influence of titanium deposition on the surface symmetry and order.

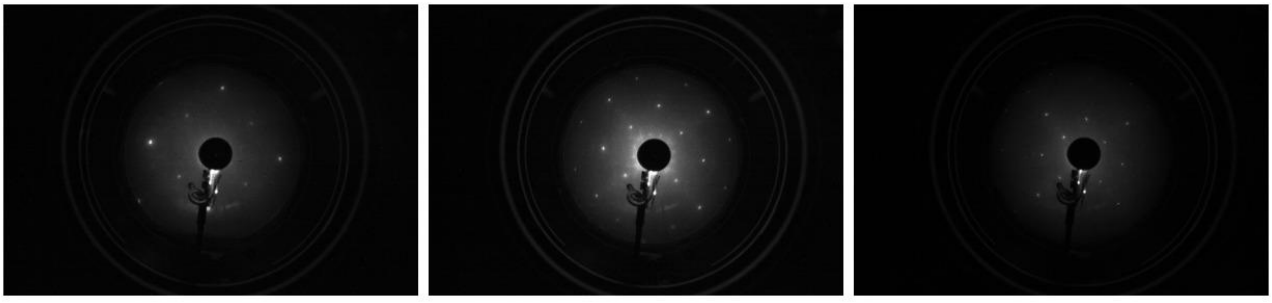

Figure 13: LEED images of the substrate STO respectively at 60, 100 and 150 eV. [56]

The quality and definition of Low-Energy Electron Diffraction patterns are strongly dependent on the energy of the incident electrons. At lower energies, such as 60 eV, the resulting images tend to be less sharp and poorly resolved compared to those obtained at higher energies, for instance at 100 eV or 150 eV. This degradation in clarity is primarily attributed to the reduced electron penetration depth at low energies, which increases the interaction of the electrons with surface features and imperfections.

Consequently, low-energy LEED is significantly more sensitive to surface-related phenomena, including the presence of adsorbates, contamination, and the finite size of surface reconstruction domains. These factors can give rise to increased diffuse scattering, thereby compromising the sharpness and contrast of the diffraction spots. In particular, poorly ordered or defective surface reconstructions tend to scatter the incident beam incoherently, resulting in a loss of definition in the LEED pattern.

Although the substrate image acquired at 150 eV may appear as if it were obtained at a lower energy due to the high brightness, we can confirm that it indeed corresponds to the higher energy, as the diffraction spots are significantly closer together compared to those observed at lower energies. The reduced brightness could be attributed to a current-related issue. The clarity and overall visibility of LEED patterns are influenced not only by the crystallographic structure of the bulk material but also by the precise atomic arrangement at the surface. At lower electron energies, specific diffraction spots may diminish in intensity or disappear entirely due to limitations in spatial coherence and the particular surface symmetry, leading to a partial or incomplete representation of the surface periodicity.

Increasing the energy of the electron beam enhances the generation of additional diffracted beams and reduces the relative impact of thermal vibrations and surface irregularities. As a result, the LEED patterns at higher energies are typically more detailed and symmetric, with a greater number of observable diffraction spots.

Thermal vibrations of surface atoms, which are more prominent at elevated temperatures, also play a critical role in determining the clarity of LEED images. Low-energy electrons are particularly susceptible to these atomic oscillations, which lead to increased inelastic scattering and a consequent blurring of the diffraction features. This thermal effect must be considered when interpreting LEED data, especially in the context of high-temperature experiments.

Strontium titanate (STO), in its pristine form, demonstrates a well-ordered and highly symmetric surface structure. This is manifested in its LEED pattern, which is characterized by intense, well-defined, and symmetrically distributed diffraction spots. Upon deposition of a titanium dioxide (TiO_2) overlayer, the intrinsic surface order of STO is perturbed. TiO_2 can

interact with the STO substrate to form a new surface phase, potentially via an epitaxial relationship, depending on the deposition conditions and lattice matching.

This newly formed structure typically exhibits a modified LEED pattern that reflects the altered surface symmetry and periodicity. The appearance of additional diffraction spots or changes in the existing pattern are indicative of a reconstructed or epitaxially grown TiO_2 layer and provide critical information regarding the surface atomic configuration and the nature of the TiO_2/STO interface.

Figure 14: LEED images of TiO_2 /STO_C26 respectively at 60, 100 and 150 eV. [56]

The Low Energy Electron Diffraction (LEED) images obtained from the TiO_2/STO_C26 sample exhibit a lower degree of definition compared to those acquired from the bare substrate. This decreased clarity can be attributed to the reduced size of the TiO_2 domains, which limits the coherence of the diffracted electron waves and results in broader and less distinct diffraction spots. Importantly, the LEED signal in this case originates exclusively from the TiO_2 overlayer, which nucleates and grows on the $SrTiO_3$ (STO) substrate.

The mismatch between the lattice parameters of the TiO_2 film and the underlying STO substrate inhibits the formation of large, continuous crystalline domains. Instead, the strain induced by this mismatch leads to the emergence of small, discrete domains with limited lateral extension. As a consequence, the diffracted intensities are broadened, and fine structural details are less resolved in the LEED pattern.

At an incident electron energy of 60 eV, the LEED pattern of the TiO_2/STO_C26 sample reveals a characteristic superstructure attributable to a two-domain overlapping 1×4 / 4×1 surface reconstruction. Although the presence of this reconstruction is evident, the broadening of the diffraction peaks and the proximity of the first-order spots to the center of the pattern (origin) indicate a relatively small domain size, consistent with the limited long-range order of the surface structure.

The formation of multiple domains with distinct orientations is necessary to preserve the

original P4mm symmetry of the STO substrate, which includes fourfold rotational symmetry (90°) and mirror planes. In scenarios where the overlayer adopts a lower symmetry, such as the 4×1 reconstruction, characterized by a periodicity ratio of 1:4 along one crystallographic axis and 1:1 along the perpendicular axis, multiple rotationally equivalent domains must coexist on the surface. This domain multiplicity effectively restores the global symmetry of the system, ensuring that the overall diffraction pattern remains consistent with the substrate's symmetry group.

The observed surface reconstruction is a well-documented feature of the anatase TiO_2 (001) surface and corresponds to a thermodynamically favorable state. This reconstruction arises as a result of surface energy minimization mechanisms and is frequently encountered in both epitaxial films and natural anatase single crystals. It reflects the intrinsic tendency of the TiO_2 (001) surface to adopt a reconstructed configuration that lowers the overall free energy of the system.

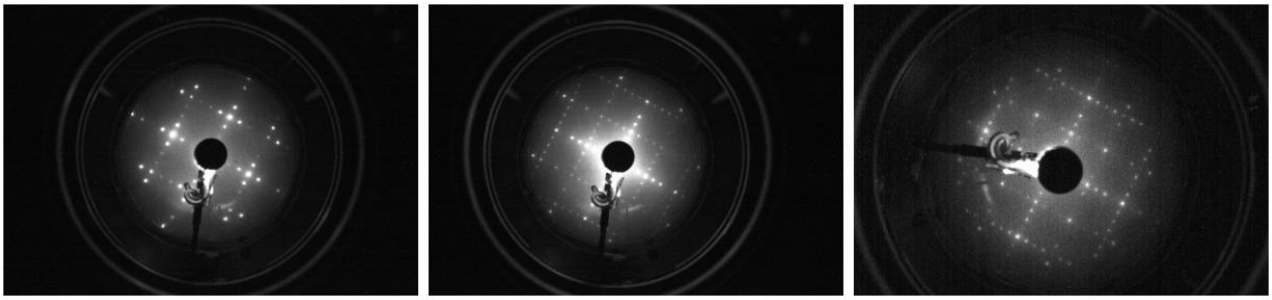

Figure 15: LEED images of $TiO_2/LaAlO_3$ respectively at 60, 100 and 150 eV. [56]

As discussed in Chapter 2, Material System, the in-plane lattice parameter (a=b) of TiO_2 in the anatase phase is 3.784 Å, while that of $SrTiO_3$ (STO) is 3.905 Å, and $LaAlO_3$ (LAO) exhibits a value of 3.787 Å. These values are critical for understanding the degree of lattice matching and the resulting epitaxial relationships at the oxide interfaces.

In the case of the $TiO_2/LaAlO_3$ heterostructure, the close match between the in-plane lattice parameters of the TiO_2 anatase layer and the LAO substrate, coupled with their compatible crystallographic orientations, leads to the formation of well-aligned and coherent interfacial domains. As a direct consequence of this structural compatibility, the LEED patterns acquired for the TiO_2/LAO system display significantly improved definition and clarity compared to those observed for the $TiO_2/SrTiO_3$ system.

The enhanced quality of the LEED images, which show sharp, well-resolved diffraction spots, can be attributed to the reduced lattice mismatch and higher degree of epitaxial registry between TiO_2 and LAO. The minimal strain at the interface facilitates the formation of larger

and more coherent crystalline domains in the TiO_2 layer, which in turn supports more constructive interference of diffracted electrons, thereby enhancing the signal-to-noise ratio and resolution in the resulting diffraction patterns.

In contrast, the greater mismatch between TiO_2 and STO introduces interfacial strain that leads to the development of smaller, less ordered domains. This structural discontinuity contributes to the observed broadening and reduced sharpness of the corresponding LEED features. Therefore, the superior definition in the LEED images of TiO_2/LAO is a direct manifestation of the favorable lattice parameter alignment and the high degree of structural coherence between the two materials.

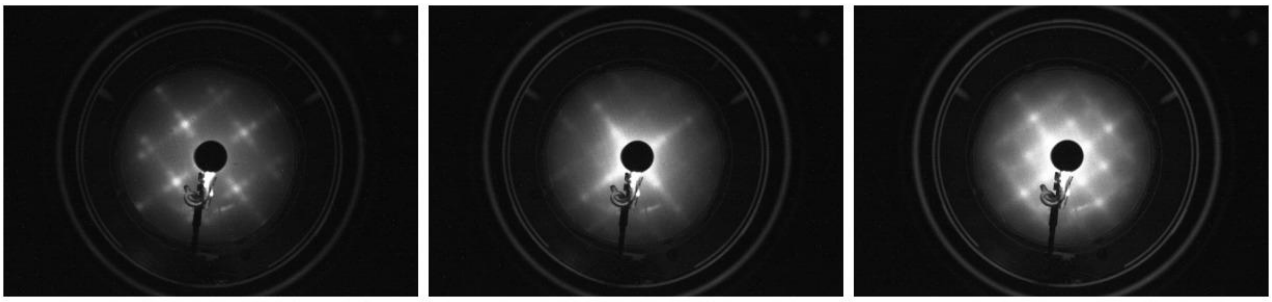

Figure 16: LEED images of Sample STO_E1 respectively at 60, 100 and 150 eV. [56]

In contrast to the pronounced differences observed in other cases, the comparison between the Low Energy Electron Diffraction (LEED) images of TiO_2 thin films grown on the STO_C26 and STO_E1 samples reveals no substantial disparity in overall image quality. The TiO_2 film deposited on the STO_C26 sample, which was grown in proximity to the oxygen cracker and therefore exposed to an atmosphere rich in atomic oxygen, displays LEED images that are only marginally better defined than those obtained from the film grown on the STO_E1 sample under molecular oxygen conditions.

The slight improvement observed in the STO_C26 sample can be attributed to the higher reactivity of atomic oxygen, which plays a more efficient role in surface oxidation processes. Atomic oxygen is known to facilitate the oxidation of titanium to higher oxidation states more effectively than molecular oxygen, thereby contributing to improved stoichiometry and surface structural order. Furthermore, atomic oxygen has the capacity to react with residual carbon contaminants on the substrate surface, forming volatile carbon monoxide (CO) that can desorb at elevated temperatures. This desorption process contributes to a cleaner and more structurally coherent surface, which is reflected in the enhanced contrast and definition in the resulting LEED patterns.

TiO_2 films grown without the intentional introduction of additional oxygen species,

particularly in molecular form, are more susceptible to the formation of oxygen vacancies and a range of other point and extended defects. These imperfections disturb the ideal periodicity of the atomic arrangement at the surface, thereby decreasing long-range order and degrading the quality of LEED images.

While the use of an oxygen cracker introduces a notable benefit in terms of surface quality enhancement via the supply of atomic oxygen, it is not devoid of drawbacks. Specifically, iridium is commonly employed as the material for the capillary in oxygen crackers due to its exceptional thermal stability and resistance to degradation under high-temperature operating conditions. However, during the operation of the cracker, where the iridium capillary is resistively heated to temperatures sufficient to dissociate O_2 molecules into atomic oxygen, there exists a non-negligible possibility of iridium atom sublimation. These atoms may condense onto the sample surface during growth, leading to trace iridium contamination.

Although the level of iridium deposition is typically minimal, it represents an unintended and undesired side effect of the cracking process. Such contamination may locally alter the surface chemistry or electronic structure of the film, which could potentially interfere with subsequent surface-sensitive analyses or device performance. Therefore, while the oxygen cracker serves a vital function in promoting high-quality film growth and enhancing surface order, its use necessitates a careful balance between the benefits of atomic oxygen exposure and the risks associated with trace metal contamination.

6.2 Analysis of Auger graphs

The interpretation of Auger Electron Spectroscopy (AES) plots, especially when comparing superimposed curves from different samples, requires careful examination of the spectral features to identify variations in chemical composition and the oxidation states of the elements present.

In the graph shown below in Figure 17, the black curve corresponds to the TiO_2/LAO sample. In this case, the characteristic peaks of lanthanum are no longer visible, likely because they are masked by the overlying oxide layer. Additionally, new peaks corresponding to titanium appear in the spectrum.

For reference, the red curve represents the bare LAO substrate, with its main peaks being La(MNN) and O(KLL). In contrast, the black curve of the TiO_2/LAO sample is dominated by O(KLL) and Ti(LMM) peaks, indicating the presence of the titanium oxide layer. To visualize

both spectra clearly, the red curve of the substrate has been shifted downward vertically. There is also a noticeable horizontal shift between the two curves. This is due to the surface of the sample with the TiO_2 film being negatively charged, which affects the kinetic energy of the emitted Auger electrons. Since electrons are being injected into the sample during analysis, the resulting negative surface charge causes the outgoing Auger electrons to accelerate slightly, increasing their energy and shifting the spectrum.

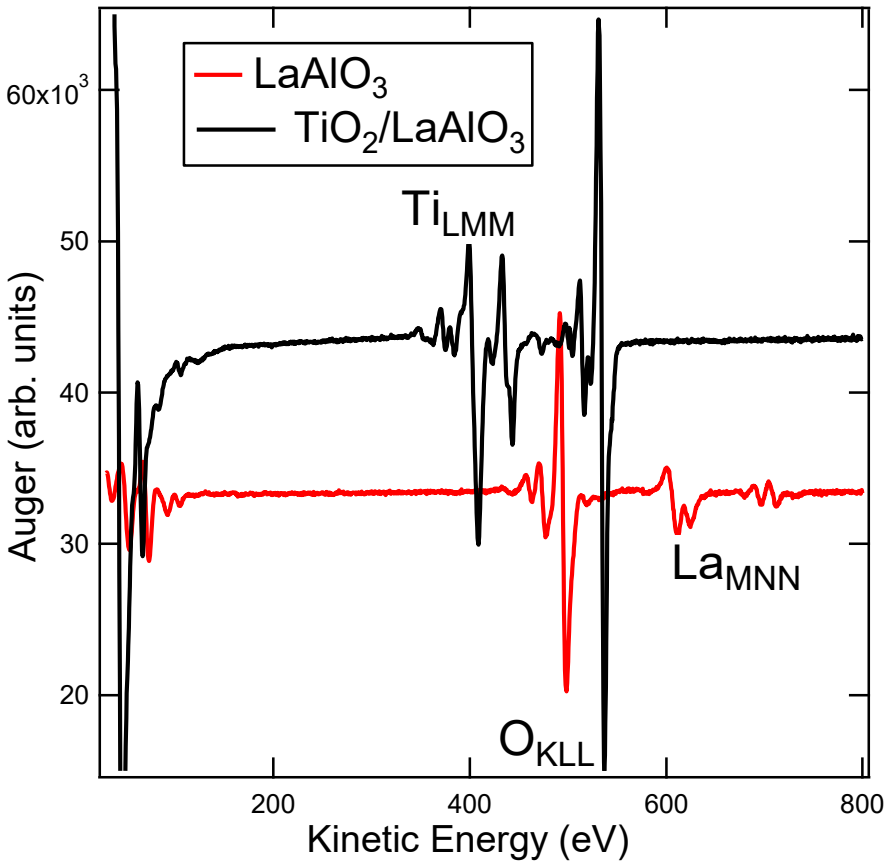

Figure 17: Auger curves of LAO and TiO_2/LAO. [56]

The sample tends to become negatively charged during Auger Electron Spectroscopy (AES), and since electrons themselves carry a negative charge, an electrostatic repulsion occurs. This repulsion causes the emitted electrons to be accelerated, which results in an increase in their kinetic energy. Consequently, the observed shift of the black curve towards higher kinetic energies is attributed to this charging effect on the sample surface.

In order to analyze and compare the AES curves of the STO substrate, the TiO_2/STO film, and the TiO_2/STO sample grown in the presence of atomic oxygen (produced by an oxygen cracker), it is important to carefully examine the specific features of the peaks related to the

elements present in each sample. This includes not only identifying the appearance or disappearance of characteristic peaks but also observing any shifts in peak positions or changes in their intensity, which can provide valuable information about differences in composition, oxidation state, and surface conditions.

In the Figure 18, the red curve, corresponding to the bare STO substrate, displays characteristic peaks associated with Sr(LMM), Ti(LMM), and O(KLL), which reflect the specific Auger energy levels of strontium, titanium, and oxygen present in the sample.

In the black curve, which refers to the TiO_2 film grown on STO, only the peaks for Ti(LMM) and O(KLL) are visible, indicating that the film covers the strontium signal, likely due to the presence of the oxide layer on the surface.

The blue curve represents the TiO_2/STO sample that was annealed in the presence of atomic oxygen using an oxygen cracker. This spectrum shows peaks for Ir(NOO), Ti(LMM), and O(KLL). The presence of iridium is attributed to the use of an iridium capillary in the oxygen cracker, which can lead to slight contamination of the surface during the annealing process.

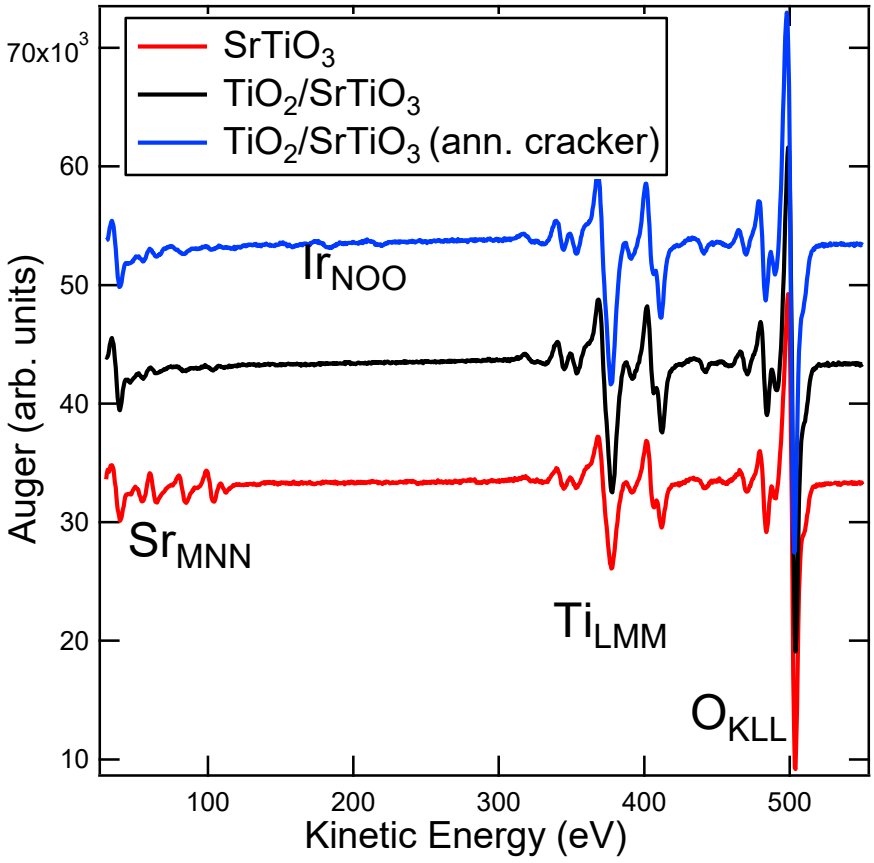

Figure 18: Auger curves of STO, TIO_2/STO and TiO_2/STO (ann. cracker). [56]

The most notable differences are that the strontium peak is visible only in the red curve of the substrate because in the others it is made invisible by the oxide film. The first peak on the left in the red curve does not correspond to strontium, whereas the other, less intense peaks do. A weak signal is also visible in the other curves. If the film is not very thick, a residual signal may be present, as the electron mean free path is on the order of nanometers. Another possibility is that the film forms islands of varying sizes, leaving some areas of the substrate exposed and thus detectable.

At low kinetic energies in the blue curve there is the peak of the (weak) iridium contamination coming from the oxygen cracker.

It should be noted that the procedure followed during the internship results in clean substrate and film surfaces, as verified by surface analysis techniques. However, trace carbon is typically detected at a kinetic energy of 272 eV (C(KLL)), which is commonly observed even under controlled conditions. This residual carbon can originate from various sources, such as the substrate itself, where it may segregate upon heating, or from the decomposition of adsorbed surface species, including carbon monoxide (CO), carbon dioxide (CO_2), and hydrocarbons, following prior exposure to air before vacuum deposition.

6.3 Analysis of XRD data

BINoculars software was used to process, compile and plot the XRD data measured at the ESRF. The main function of this software is to make a coordinate transformation to represent the diffracted intensity in the reciprocal (hkl) space instead of the original diffractometer angles space.

The two-dimensional X-ray detector has a small surface compared to the LEED screen, but the surface corresponds to portions of reciprocal lattice space.

In data analysis, each detector pixel is linked to a specific location in reciprocal space, based on the known scattering geometry, the detector's distance from the sample, and the physical dimensions of the detector.

Among the different samples to be analyzed was chosen the sample named X17_CTR which was grown by co-supervisor Xavier Torrelles in his laboratory. The X17_CTR sample was obtained with the thin film deposition technique (about 50 nm) called Pulsed Laser Deposition (PLD). This sample was annealed in situ at 800°C in 10^-6 mbar O2. This, as we will see, allows to recover the original (4x1) reconstruction. To verify the surface reconstruction on the sample, scans were performed in suitable reciprocal space regions.

The software treats all the files that were sent to it as input and measures each intensity of each pixel of the detector screen and reconstructs which Miller index corresponds then adds up when the Miller indices are equal and finally takes an average; by executing the procedure, one acquires an image that reflects the measured data.

An averaging operation is carried out for each scan because the same (hkl) reflection may appear multiple times within a single scan. To account for this redundancy, the intensity values associated with identical (hkl) indices are averaged, resulting in a single representative intensity for each unique reflection. This step helps to simplify and consolidate the data while preserving its essential features.

The visualization and generation of the resulting images were performed using the BINoculars-gui software.

Figure 19 shows a projection taken perpendicular to the Miller index L. On the right side of the image, a multicolour vertical stripe indicates the intensity scale, which is normalized with

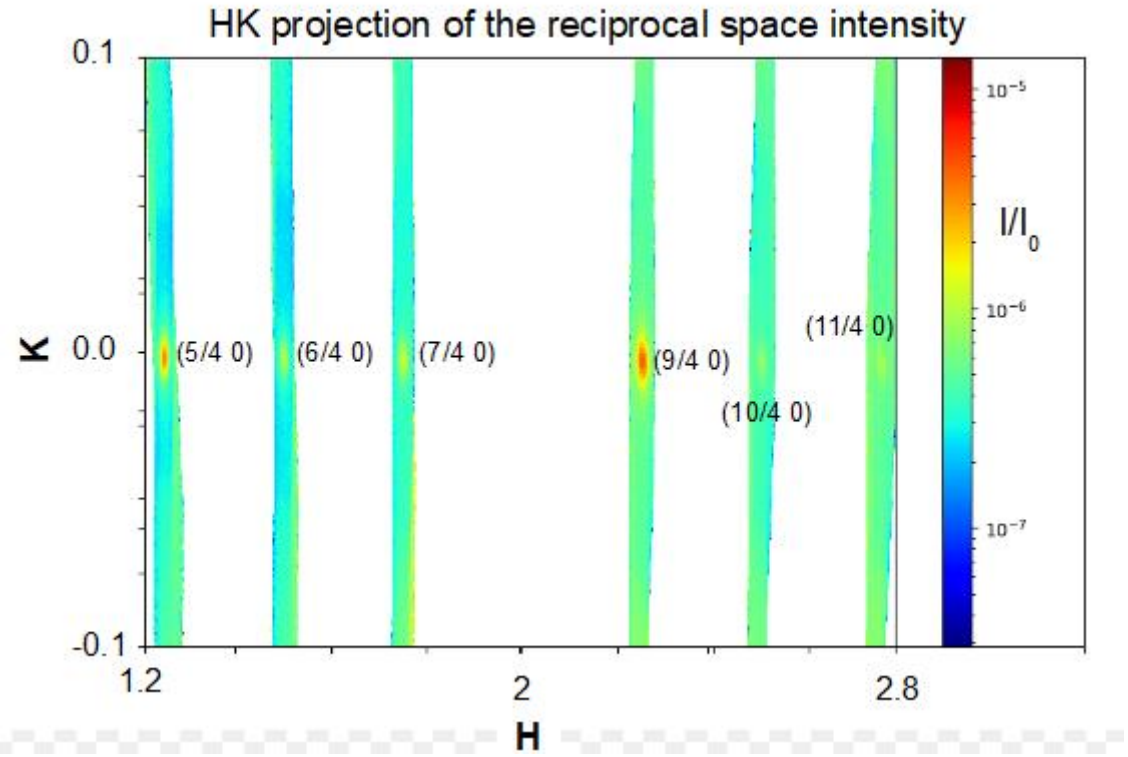

Figure 19: XRD data in the HK projection. [57]

respect to the incident beam intensity, noted as I_0. At K=0 where the intensity is maximum, points are shown which correspond to the LEED diagrams.

In contrast, Figure 20 shows a projection taken perpendicular to the Miller index K. In this case, for L=0, the discrete points are no longer present. Instead, central lines appear, representing the distribution of intensity along the L direction. This situation is somewhat

analogous to varying the energy in a LEED experiment, which effectively increases the radius of the Ewald sphere, here manifested by an increasing L index for a fixed (H, K) reflection. This behavior suggests that the observed reconstruction originates from a region of limited extent in the direction perpendicular to the surface.

From these X-diffraction images is possible to see the same reconstruction that is seen in LEED. Mapping a large portion of reciprocal space with this technique, however, is time consuming, while a LEED image is collected at one. The measurements obtained using LEED and XRD techniques can reveal the same (4×1) surface reconstruction observed on the anatase (001) surface. However, each method has distinct sensitivities and resolutions, arising from the nature of the employed probes and their respective sampling depths. In Figure 18, the features at K=0 correspond to the surface reconstructions that appear as bright spots in LEED. In XRD, these features are less pronounced because XRD is primarily used to study the bulk structure rather than surface topography, as is the case with LEED.

It is not a case that after the abscissa points equal to 2 the intensity increases, and this depends on the structure. From these measurements it is possible to make a model of the surface because in X-rays it is much simpler to make a model, the intensity is easier to calculate than with electrons. While Bragg peaks are not sensitive to surface contamination the same is not true for surface peaks like the (4x1) reconstruction.

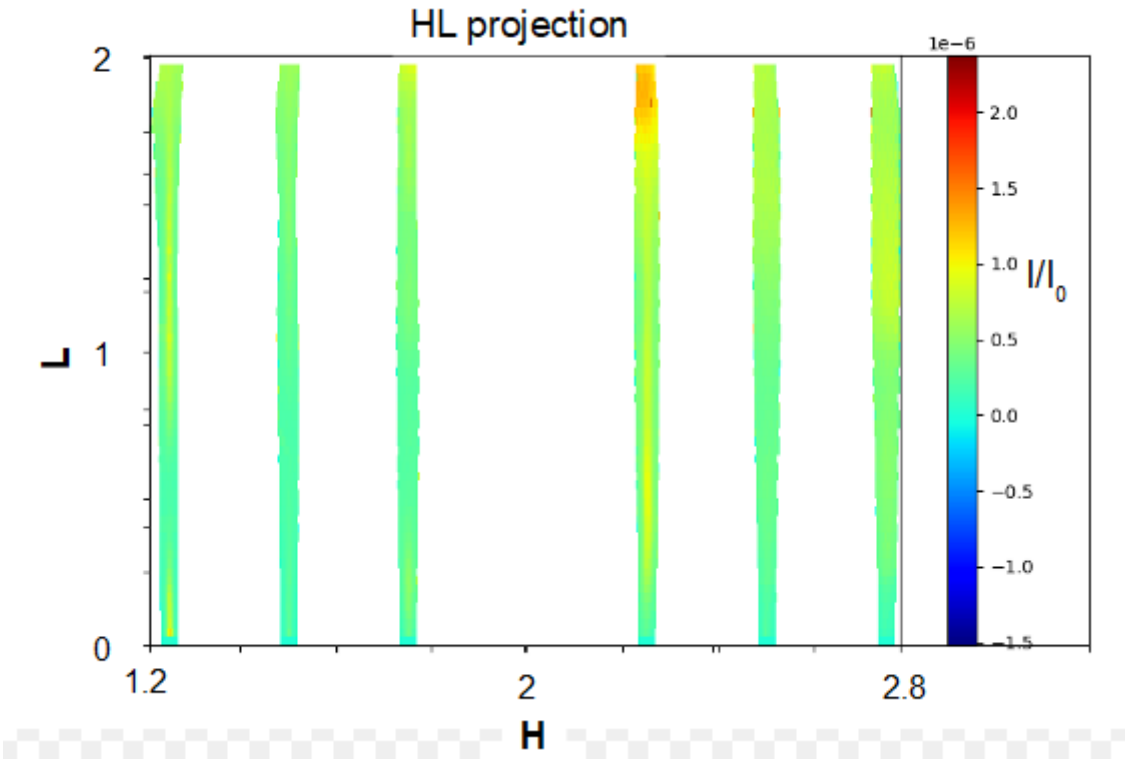

Figure 20: XRD data in the HL projection [57]

Figure 21 displays the Bragg peak. The Bragg peaks originating from the film are clearly visible and appear as very intense and sharp features when compared to the broader surface peaks. It's important to note that the width of a Bragg peak is inversely related to the film's thickness, meaning that a thicker film will result in narrower peaks. Since the reconstruction occurs only at the surface level, the corresponding peaks are associated with just 2 or 3 monolayers, making them much more diffuse.
Therefore, simply by observing the width of the peak, one can already get an idea of the film thickness or estimate how many layers are involved in the reconstruction.

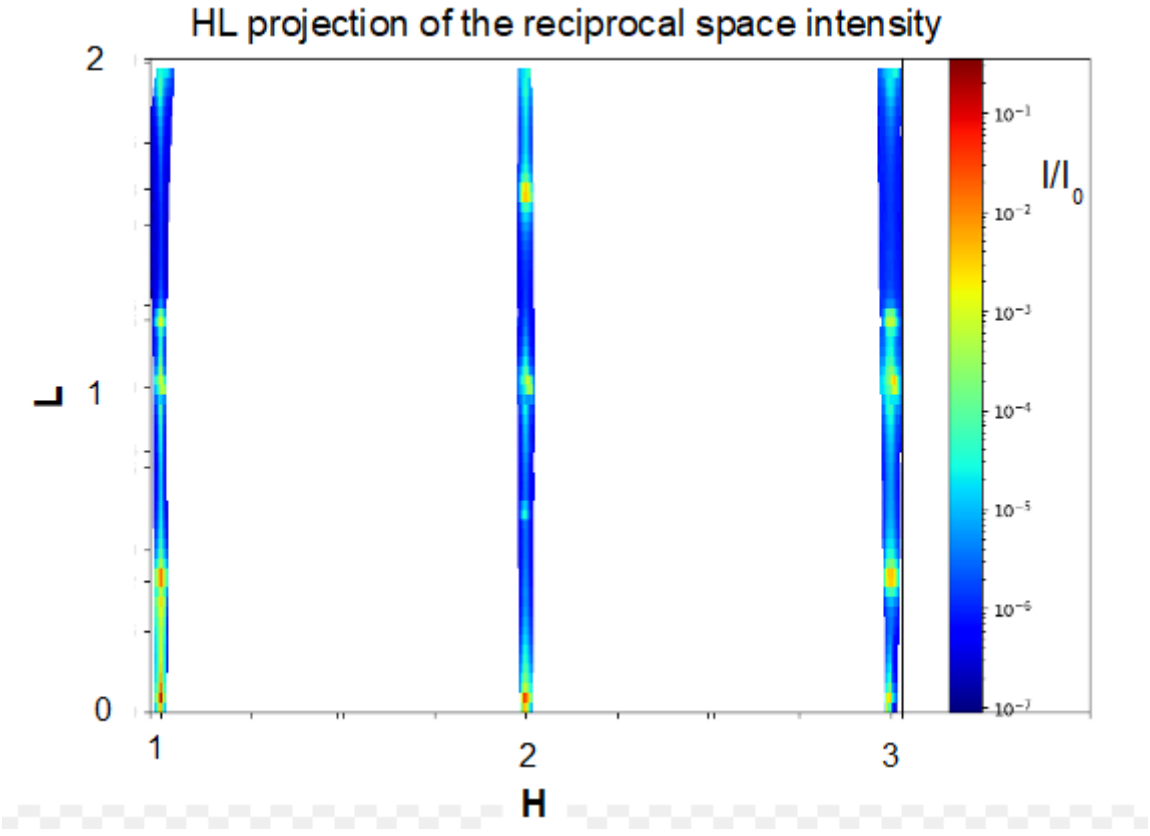

Figure 21: High intensities XRD data in the HL projection. [57]

The surface peaks detected using synchrotron radiation are extremely weak and would be practically undetectable with conventional laboratory X-ray sources. This is because their intensity is simply too low to register under normal lab conditions. As a result, the peaks shown in Figures 19 and 20 would not be observable in a standard laboratory setup, since their signal is approximately 100.000 times weaker than the intensity range displayed in the scale of Figure 21.

7 Conclusion

This six-month internship focused on the growth and characterization of TiO_2-anatase (001) on $SrTiO_3$ and $LaAlO_3$ substrates using Molecular Beam Epitaxy (MBE). The goal was to understand how different substrates and growth conditions affect the film's structure, with potential applications in photocatalysis. The films were deposited on $SrTiO_3$ and $LaAlO_3$ substrates, with parameters such as temperature and oxygen pressure being optimized to enhance film quality.

LEED images confirmed that the TiO_2-anatase (001) thin films grew epitaxially on both $SrTiO_3$ and $LaAlO_3$ substrates, closely matching the crystal structure of the underlying materials. For the clean substrates, the LEED patterns displayed clear, well-resolved spots, matching the expected bulk crystal configurations. This demonstrated that the surfaces were highly ordered following annealing and confirmed the efficacy of the substrate preparation process. When analyzing the TiO_2-anatase films, changes in the LEED patterns indicated the development of a new surface periodicity due to the presence of the TiO_2 overlayer. By varying the energy of the electron beam, it was possible to probe different surface depths and gain more detailed information. One of the findings was the appearance of a (4×1) surface reconstruction, a well-known feature of TiO_2-anatase (001) surfaces. The reconstruction reduces this energy by reorganizing the atoms into a more stable pattern.

The substrate played a significant role in determining the structural quality of the TiO_2 films. On $SrTiO_3$, due to its 3% mismatch with TiO_2, the LEED images showed broader spots, pointing to smaller and possibly more disordered surface domains. Nevertheless, the (4×1) reconstruction was still present. On $LaAlO_3$, which has a near-perfect match, sharper LEED spots indicated a more ordered and coherent film growth.

Furthermore, the Auger spectrum provided detailed information on the chemical composition of the films, showing the presence of titanium, oxygen and traces of iridium, as well as their oxidation state. This data was fundamental to understanding the surface properties of TiO2-anatase films, in particular defects, contaminants and interactions between the different zones of the material.

Variations in deposition parameters, such as substrate temperature, oxygen pressure during deposition, and the use of oxygen crackers, significantly influence film quality and properties. For instance, oxygen crackers enhance film quality by promoting atomic oxygen availability, which improves surface oxidation and reduces defects.

The surface reconstructions observed in TiO_2-anatase films, such as the 1x4/4x1 pattern,

are consistent with previous theoretical and experimental expectations regarding the compatibility of lattice parameters.

Future work could explore additional substrates, advanced characterization techniques, and the integration of these films into functional devices.

Bibliography

[1] M. Lazzeri, A. Selloni - Stress-Driven Reconstruction of an Oxide Surface: The Anatase TiO2 (001) - (1 x 4) Surface), PhysRevLett, 87, 26, (2001)

[2] G. Li, K. Fang, et al. - Surface study of the reconstructed anatase TiO2 (001) surface, Prog. Nat. Sci.: Mater. Int., 31, 2, (2020)

[3] Qu'est-ce que l'institut Néel: Historique [online]. Available on: https://neel.cnrs.fr/institut-neel/quest-ce-que-linstitut-neel/historique

[4] F. Parrino, L. Palmisano, G. Korotcenkow - Titanium Dioxide (TiO_2) and Its Applications, Elsevier, 2, 13-16 (2020).

[5] D. Filippou, G. Hudon - Iron removal and recovery in the titanium dioxide feedstock and pigment industries, JOM, 61, 36-42, (2009)

[6] B. Wei, et al. - Understanding the Role of Rutile TiO_2 Surface Orientation on Molecular Hydrogen Activation, Nanomaterials, 9, 1199, (2019)

[7] D. R. Eddy, et al. - Heterophase Polymorph of TiO_2 (Anatase, Rutile, Brookite, TiO2 (B)) for Efficient Photocatalyst: Fabrication and Activity, Nanomaterials 2023, 13(4), 704, (2023)

[8] G. Sivalingam, K. Nagaveni, M.S. Hegde, et al. - Photocatalytic degradation of various dyes by combustion synthesized nano anatase TiO_2, Appl. Catal. B Environ., 45, 23-38, (2003)

[9] Michele Lazzeri, Andrea Vittadini, and Annabella Selloni - Structure and energetics of stoichiometric TiO2 anatase surfaces, Phys. Rev. B, 65, 119901, (2002)

[10] J. Liu, et al. - A Simple Route to Prepare Anatase TiO2 Films with Dominant (001) facet, Mater. Lett., 318, 132225, (2022)

[11] K. Bourikas, C. Kordulis, A. Lycourghiotis - Titanium Dioxide (Anatase and Rutile): Surface Chemistry, Liquid - Solid Interface Chemistry, and Scientific Synthesis of Supported Catalysts, Chem. Rev., 114, 19, 9754-9823, (2014)

[12] S. E. Reyes-Lillo, K. M. Rabe, J. B. Neaton - Ferroelectricity in [111]-oriented epitaxially strained SrTiO3 from first principles, Phys. Rev. Materials 3, 030601, (2019)

[13] Image available on: https://www.semanticscholar.org/paper/STRONTIUM-TITANATE-11-2-.-1-Properties-of-strontium/061cbbc202270e6e1aec175c01587f4d0dadda3d

[14] F. Alarab, et al. - Study and characterization of SrTiO3 surface, AIP Conf. Proc., 1996, 020001, (2018)

[15] M. Son, et al. - Optimizing surface treatment for Nb-doped SrTiO3 substrates: effects on structural and chemical properties, J. Korean Phys. Soc, 85, 183-191, (2024)

[16] E. A. Steele - Surface Characterization of Lanthanum Aluminate, Thesis, Northwestern University, 2016). Available on:
https://www.numis.northwestern.edu/thesis/Steele_thesis.pdf

[17] M. Yaseen, etc. - Investigation of LaAlO3 perovskite compound for optoelectronic and thermoelectric devices under pressure, Mater. Res. Express, 7, 015907, (2020)

[18]: photo taken by me.

[19] LAO (LaAlO3) Lanthanum Aluminate Crystal Substrates (5pack). Available on: https://www.crystalsubstrates.com/products/lanthanum-aluminate-lao-laalo3-substrates

[20] M. Yang, et al. - Coexistence of surface oxygen vacancy and interface conducting states in LaAlO3/SrTiO3 revealed by low-angle resonant soft X-ray scattering (2023). DOI:10.48550/arXiv.2306.05608

[21] R. Jenkins - X-Ray Analysis, Acad. Press., Third Edition, 887-902, (2003)

[22] S. Mogk - Auger Electron Spectroscopy, Montana State University, 2021. Available on: https://serc.carleton.edu/msu_nanotech/methods/aes.html

[23] P. K. Chu - Auger Electron Spectroscopy, City University of Hong Kong. Available on: https://www.cityu.edu.hk/phy/appkchu/AP5301/Lecture-10-AES.pdf)

[24] D. J. O'Connor, B. A. Sexton, et al. - Surface Analysis Methods in Materials Science (2nd Edition), Springer, 13, 275-288, (2003)

[25] W. Moritz, M. A. Van Hove - Surface Structure Determination by LEED and X-rays, Cambridge Univ. Press, 1, 2-3, (2022)

[26] R. Nix - Low Energy Electron Diffraction (LEED), Queen Mary University of London. Available on:

https://chem.libretexts.org/Bookshelves/Physical_and_Theoretical_Chemistry_Textbook_Maps/Surface_Science_(Nix)/06%3A_Overlayer_Structures_and_Surface_Diffraction/6.02%3A_Low_Energy_Electron_Diffraction_(LEED)

[27] Photo taken by me.

[28] Low Energy Electron Diffraction (LEED). Available on: http://www.ocivm.com/_low_energy_electron_diffraction.html

[29] D. Menzel, et al. - A low-energy electron diffraction data acquisition system for very low electron doses based upon a slow scan charge coupled device camera, Rev. Sci. Instrum. 67, 378-383, (1996)

[30] V. N. Strocov et al. - Concept of a multichannel spin-resolving electron analyzer based on Mott scattering, J Synchrotron Radiat., 22 (3), 708-716, (2015)

[31] ViPErLEED. Available on: https://github.com/viperleed

[32] M. Schmid, et al. - ViPErLEED package II: Spot tracking, extraction, and processing of I(V) curves, Phys. Rev. Research 7, 013006, (2025)

[33] Z. R. Robinson - Influence of Chemisorbed Oxygen on the Growth of Graphene on Cu(100) by Chemical Vapor Deposition, J. Phys. Chem. C, 117, 23919, (2013)

[34] P. Zieliński - Review of Surface Relaxation and Reconstruction Phenomena, Acta Phys. Pol. A., 89, 251-263, (1996)

[35] Slide 10/24 available on: https://slideplayer.com/slide/8868017/#google_vignette

[36] N. Perez - Phase Transformation in Metals, Springer, 2, 45-74, (2020)

[37] A. Y. Cho - Molecular Beam Epitaxy (key Papers In Applied Physics), AIP Press, (1994)

[38] H. Asahi - Molecular Beam Epitaxy: Materials and Applications for Electronics and Optoelectronics, Wiley, (2019)

[39] A. J. Ptak - Principles of Molecular Beam Epitaxy, NH, 4, 161-192, (2015)

[40] The Molecular-Beam Epitaxy (MBE) Process. Available on: https://resources.pcb.cadence.com/blog/2024-the-molecular-beam-epitaxy-mbe-process

[41] F. Lévy - Film Growth and Epitaxy: Methods, ECMP, 2, 210-222, (2005)

[42] C. Julian Chen - Introduction to Scanning Tunneling Microscopy (Third Edition), OUP, 1, 72, (2021)

[43] G. Binnig, Heinrich Rohrer - Scanning tunneling microscopy from birth to adolescence, Rev. Mod. Phys, 59, 615, (1987)

[44] Image available on: https://scienceinfo.com/scanning-tunneling-microscope/

[45] F. Adams - X-RAY ABSORPTION AND DIFFRACTION, Encycl. Anal. Sci., 9, 365-378, (2005)

[46] M. Lee - X-RAY DIFFRACTION FOR MATERIALS RESEARCH From Fundamentals to Applications, AAP, 1, 15, (2016)

[47] X-ray Diffraction (XRD). Available on: https://app.jove.com/v/10446/x-ray-diffraction-for-determining-atomic-and-molecular-structure

[48] J. R. Connolly - Introduction to X-Ray Powder Diffraction, Spring, (2005). Available on: https://www.ocf.berkeley.edu/~mwg/lab/xdocs/pxrdintro.pdf

[49] M. Ermrich, D. Opper - XRD for the analyst: Getting acquainted with the principles, PANalytical, 9.3, 78, (2011)

[50] ESRF - ABOUT US. Available on: https://www.esrf.fr/about

[32] John C. Vickerman and Ian S. Gilmore - Surface Analysis - The Principal Techniques (2009, John Wiley & Sons, Ltd)

[33] How does a synchrotron work? Available on: https://www.esrf.fr/home/education/what-is-the-esrf/how-does-the-esrf-work.html

[34] Ángeles G. De la Torre, etc - Synchrotron X-ray Diffraction in Mineralogy and MaterialsChemistry. Possibilities and Applications (2009,Universidad de Málaga)
birth to adolescence, Rev. Mod. Phys, 59, 615, (1987)

[44] Image available on: https://scienceinfo.com/scanning-tunneling-microscope/

[45] F. Adams - X-RAY ABSORPTION AND DIFFRACTION, Encycl. Anal. Sci., 9, 365-378, (2005)

[46] M. Lee - X-RAY DIFFRACTION FOR MATERIALS RESEARCH From Fundamentals to Applications, AAP, 1, 15, (2016)

[47] X-ray Diffraction (XRD). Available on: https://app.jove.com/v/10446/x-ray-diffraction-for-determining-atomic-and-molecular-structure

[48] J. R. Connolly - Introduction to X-Ray Powder Diffraction, Spring, (2005). Available on: https://www.ocf.berkeley.edu/~mwg/lab/xdocs/pxrdintro.pdf

[49] M. Ermrich, D. Opper - XRD for the analyst: Getting acquainted with the principles, PANalytical, 9.3, 78, (2011)

[50] ESRF – ABOUT US. Avalable on: https://www.esrf.fr/about

[51] J. C. Vickerman, I. S. Gilmore - Surface Analysis - The Principal Techniques, Wiley, 8.3, 424-456, (2009)

[52] How does a synchrotron work? Available on: https://www.esrf.fr/home/education/what-is-the-esrf/how-does-the-esrf-work.html

[53] Á. G. De la Torre, etc - Synchrotron X-ray Diffraction in Mineralogy and Materials and Chemistry. Possibilities and Applications, 6, (2009)

[54] Data taken in lab.

[55] Ding, Y., Weindl, P., Lenz, AG. et al. Quartz crystal microbalances (QCM) are suitable for real-time dosimetry in nanotoxicological studies using VITROCELL®Cloud cell exposure systems. Part Fibre Toxicol 17, 44, (2020)

[56] Graphs taken in Néel laboratory.

[57] Data taken from Binoculars softwareware.